01 Aug 2015

Strain Distribution and Crack Detection in Concrete Overlays with Pulse Pre-Pump Brillouin Optical Time Domain Analysis

Yi Bao

Genda Chen
Missouri University of Science and Technology, gchen@mst.edu

MID-AMERICA TRANSPORTATION CENTER

Report # MATC-MS&T: 292

Final Report
WBS: 25-1121-0003-292

Strain Distribution and Crack Detection in Concrete Overlays with Pulse Pre-Pump Brillouin Optical Time Domain Analysis

Yi Bao
Ph.D. Candidate
Department of Civil, Architectural, and Environmental Engineering
Missouri University of Science and Technology

Genda Chen, Ph.D., P.E., F.ASCE
Professor and Robert W. Abbett Distinguished Chair in Civil Engineering
Director, System and Process Assessment Research Laboratory
Associate Director, Mid-America Transportation Center
Department of Civil, Architectural, and Environmental Engineering
Missouri University of Science and Technology

2015

A Cooperative Research Project sponsored by
U.S. Department of Transportation-Research
and Innovative Technology Administration

Strain Distribution and Crack Detection in Concrete Overlays with Pulse Pre-Pump Brillouin Optical Time Domain Analysis

Yi Bao, Ph.D. Candidate
Department of Civil, Architectural, and Environmental Engineering
Missouri University of Science and Technology

Genda Chen, Ph.D., P.E., F.ASCE
Professor and Robert W. Abbett Distinguished Chair in Civil Engineering
Director, System and Process Assessment Research Laboratory
Associate Director, Mid-America Transportation Center
Department of Civil, Architectural, and Environmental Engineering
Missouri University of Science and Technology

A Report on Research Sponsored by

Mid-America Transportation Center

University of Nebraska-Lincoln

August 2015

Technical Report Documentation Page

1. Report No. 25-1121-0003-292	2. Government Accession No.	3. Recipient's Catalog No.
4. Title and Subtitle Strain Distribution and Crack Detection in Concrete Overlays with Pulse Pre-Pump Brillouin Optical Time Domain Analysis		5. Report Date August 2015
		6. Performing Organization Code
7. Author(s) Yi Bao and Genda Chen		8. Performing Organization Report No. 25-1121-0003-292
9. Performing Organization Name and Address Mid-America Transportation Center 2200 Vine St. PO Box 830851 Lincoln, NE 68583-0851		10. Work Unit No. (TRAIS)
		11. Contract or Grant No.
12. Sponsoring Agency Name and Address Research and Innovative Technology Administration 1200 New Jersey Ave., SE Washington, D.C. 20590		13. Type of Report and Period Covered July 2013 – February 2015
		14. Sponsoring Agency Code MATC TRB RiP No. 34782
15. Supplementary Notes		

16. Abstract

This report is focused on the measurement of strain distributions and crack detection in unbonded and bonded pavement overlays. The main objectives of this study are: (a) to characterize the strain sensing properties of distributed fiber optic sensors with recently-developed pulse pre-pump Brillouin optical time domain analysis (PPP-BOTDA), (b) to develop an installation method for real world applications, (c) to document the performance of the PPP-BOTDA technology in unbonded/bonded pavement applications, and (d) to develop a numerical model to facilitate the analysis of mechanical behavior of unbonded pavement overlay under vehicle wheel loads. A thin concrete layer can be cast on top of a severely deteriorated pavement layer with a fabric sheet in between to rapidly and cost-effectively improve the driving condition of existing roadways. Once cured, the concrete layer is divided into many panels and often referred to as the unbonded Portland cement concrete (PCC) overlay. The service life of PCC overlays can be appreciably extended by appropriate rehabilitation strategies at early stages of deterioration based on the information provided by health monitoring. The strain distribution and crack detection are of interest to engineers in this application. Minor or moderately deteriorated existing concrete pavements can also be resurfaced with a thin concrete layer to improve their driving condition. In this case, potential cracks in the existing pavement may easily penetrate through the new concrete layer. The way the potential slip at their interface develops over time is an interesting question to answer. This study reports an application of a commercial single mode optical fiber to measure strain distributions in full-scale fiber reinforced unbonded overlays. Prefabricated cementitious mortar grid instrumented with distributed fiber optic sensors, namely smart grid, was developed and proposed to address the logistics of handling delicate optical fibers, and thus facilitate the in-situ construction. The smart grids can be laid on top of the fabric sheet and embedded in concrete overlay. With the proposed method, the pavement overlays instrumented with distributed sensors were successfully constructed in Minnesota's Cold Weather Road Research Facility (MnROAD). The optical fibers were characterized on a precision load frame at room temperature. A Neubrescope was used to measure strain distributions based on the pulse pre-pump Brillouin optical time domain analysis (PPP-BOTDA). The overlays were subjected to repeated truck loads and eventually cracked. Strain distributions were obtained from the distributed fiber optic sensor. Cracks were identified and localized by mapping the strain distribution in which the sharp peaks represent the cracks. The strain distribution was further investigated using a three-dimensional finite element model incorporating nonlinear boundary conditions. Opening between substrate and overlay concrete was demonstrated, and strain distributions in overlay and substrate concrete were determined with the numerical model. For the bonded concrete overlays on existing pavement, a delamination detection method was developed and implemented using the distributed fiber optic sensors. Delamination can be identified as sharp peaks in the measured strain distributions.

17. Key Words Add key words here	18. Distribution Statement		
19. Security Classif. (of this report) Unclassified	20. Security Classif. (of this page) Unclassified	21. No. of Pages 79	22. Price

Table of Contents

List of Figures

List of Tables

Acknowledgements

Financial support was provided by Mid-America Transportation Research Center under contract agreement No. 25-1121-0003-292. Thanks are due to Dr. Kamal H. Khayat and his student, Mr. Mahdi Valipour, for their collaboration in the study of bond behaviour between an existing substrate and its fresh overlay.

Disclaimer

The contents of this report reflect the views of the authors, who are responsible for the facts and the accuracy of the information presented herein. This document is disseminated under the sponsorship of Mid-America Transportation Research Center, in the interest of information exchange. Mid-America Transportation Research Center assumes no liability for the contents or use thereof.

Executive Summary

This report summarizes the results and findings of a Mid-America Transportation Research Center (MATC) research project No. 25-1121-0003-292. It is focused on the measurement of strain distributions and crack detection in unbonded and bonded pavement overlays. The main objectives of this study are: (a) to characterize the strain sensing properties of distributed fiber optic sensors with recently-developed pulse pre-pump Brillouin optical time domain analysis (PPP-BOTDA), (b) to develop an installation method for real world applications, (c) to document the performance of the PPP-BOTDA technology in unbonded/bonded pavement applications, and (d) to develop a numerical model to facilitate the analysis of mechanical behaviour of unbonded pavement overlay under vehicle wheel loads.

A thin concrete layer can be cast on top of a severely deteriorated pavement layer with a fabric sheet in between to rapidly and cost-effectively improve the driving condition of existing roadways. Once cured, the concrete layer is divided into many panels and often referred to as the unbonded Portland cement concrete (PCC) overlay. The service life of PCC overlays can be appreciably extended by appropriate rehabilitation strategies at early stages of deterioration based on the information provided by health monitoring. The strain distribution and crack detection are of interest to engineers in this application.

Minor or moderately deteriorated existing concrete pavements can also be resurfaced with a thin concrete layer to improve their driving condition. In this case, potential cracks in the existing pavement may easily penetrate through the new concrete layer. The way the potential slip at their interface develops over time is an interesting question to answer.

This study reports an application of a commercial single mode optical fiber to measure strain distributions in full-scale fiber reinforced unbonded overlays. Prefabricated cementitious

mortar grid instrumented with distributed fiber optic sensors, namely smart grid, was developed and proposed to address the logistics of handling delicate optical fibers, and thus facilitate the *in-situ* construction. The smart grids can be laid on top of the fabric sheet and embedded in concrete overlay. With the proposed method, the pavement overlays instrumented with distributed sensors were successfully constructed in Minnesota's Cold Weather Road Research Facility (MnROAD). The optical fibers were characterized on a precision load frame at room temperature. A Neubrescope was used to measure strain distributions based on the pulse pre-pump Brillouin optical time domain analysis (PPP-BOTDA). The overlays were subjected to repeated truck loads and eventually cracked. Strain distributions were obtained from the distributed fiber optic sensor. Cracks were identified and localized by mapping the strain distribution in which the sharp peaks represent the cracks. The strain distribution was further investigated using a three-dimensional finite element model incorporating nonlinear boundary conditions. Opening between substrate and overlay concrete was demonstrated, and strain distributions in overlay and substrate concrete were determined with the numerical model.

For the bonded concrete overlays on existing pavement, a delamination detection method was developed and implemented using the distributed fiber optic sensors. Delamination can be identified as sharp peaks in the measured strain distributions.

Chapter 1 Introduction

Unbonded Portland cement concrete (PCC) overlays have received increasing attention in new highway constructions and existing pavement rehabilitations (Ioannides and Sengupta 2003, Liao 2011, Burnham 2013). Thin PCC overlays have been cast on top of an existing pavement with a separation fabric layer to prevent the propagation of reflection cracking that has been observed in bonded concrete overlays. However, they can be more vulnerable to cracking than thick overlays due to reduced thickness and thus increased strain under the same vehicle load. Cracks can potentially accelerate the deterioration and reduce the service life of concrete pavements (Raoufi 2010). Therefore, strain measurement and crack detection are critically important in the maintenance and management of U.S. paved highway roads (Zhang et al. 2014), which exceed 4 million km in length according to the Bureau of Transportation Statistics in the United States Department of Transportation (USDOT 2014).

Point or localized sensing and non-destructive evaluation technologies have been developed to monitor strain and cracking in concrete structures. For example, vibrating wires and fiber Bragg gratings (FBG) were embedded in concrete pavement to measure strains and, by identifying sudden jumps in the strain measurements, perhaps detect one or more cracks when they happen to cross the sensors over their gauge length (Azenha et al. 2009, Lu and Xie 2007, Stephen 2012). Multiple FBG sensors were connected in series and multiplexed to increase the likelihood of crack detection with a so-called quasi-distributed fiber optic sensor (Zhao and Ansari 2001). In general, the point sensors have three disadvantages: (i) low in success rate for the detection of unknown cracks, (ii) costly for a long distance deployment of highway roads, and (iii) inaccurate in strain measurement in thin pavement overlays since the dimension of sensors is often comparable with the overlay's thickness, and thus the presence of the sensors can

alter the strain field to be measured. Acoustic emission (AE) was also used to detect cracking in concrete structures (Ouyang et al. 1991). However, AE signals are very noisy and thus highly depend on the design of noise filters in data interpretation.

Distributed sensing technology may be advantageous over the point sensing and non-destructive evaluation technologies. For example, coaxial cable sensors were invented and successfully applied to measure strain distributions and detect a wide range of cracks, from visually invisible to excessive corresponding to the failure of a full-scale reinforced concrete girder (Chen et al. 2005). However, coaxial cable sensors are presently unavailable in market and their measurement is potentially affected by passing vehicles on highways since the electromagnetic signals travelling in the cables are not immune to electromagnetic interference (EMI). Considering these constraints, distributed fiber optic sensors are likely a better choice for this application due to cost effectiveness, EMI immunity, and robustness in harsh environments (Bao and Chen 2011, 2012).

Light scattering-based sensing technologies provide excellent opportunities for distributed sensing of strain and temperature along an optical fiber (Bao and Chen 2011, 2012). Due to the advantages, such as large measurement range and continuous sensing ability besides reduced size and weight, EMI immunity, and robustness in harsh environment, fully distributed optical fiber sensors have attracted intensive research interest worldwide and are being studied and successfully applied in various research areas. The technology can be implemented in various applications such as strain distributions or crack detection in civil engineering structures, ground settlement or sliding damage monitoring, and detection of pipeline leaking or buckling (Bernini et al. 2007).

Light propagating in the form of an oscillating electromagnetic field interacts with the

atoms and molecules of an optical fiber. When its wavelength is not in resonance with that of the medium, the electric field induces a time-dependent polarization dipole. The induced dipole generates a secondary electromagnetic (EM) wave, called Rayleigh, Brillouin, or Raman scattering (Bao and Chen 2011, 2012). Rayleigh scattering is a linear scattering process in which the scattered power is simply proportional to the incident power. Since no energy is transferred to the optical fiber in Rayleigh scattering, the frequency of the scattered light remains the same as that of the incident light, which is referred to as elastic scattering. It is attributed to non-propagating density fluctuations. In figure 1.1, the two lines located immediately on the two sides of the Rayleigh peak represent Brillouin scattering. They are contributed by the scattering of sound waves moving in opposite directions. The left peak with a downshifted frequency is called the Stokes peak, while the right one with an up-shifted frequency is called the anti-Stokes peak. Raman scattering is contributed by the interaction of the light wave with molecular vibration in the medium. Both Brillouin and Raman scatterings are inelastic because they are associated with frequency shifts. The last mechanism that can be observed is the Rayleigh wing scattering attributed to fluctuations in the orientation of anisotropic molecules. Raman spectra usually contain many sharp bands separated by the electronic vibration, each resulting from molecular rotation or reorientation excitations (Bao and Chen 2011, 2012). Spontaneous scattering means that the input light is scattered without significantly changing the optical properties of the medium, including Rayleigh scattering, Brillouin scattering, and Raman scattering. Otherwise, when the light intensity increases to a level, if the properties of the medium are modified and the scattered light is proportional to the power of the input light, this regime becomes stimulated and the scattering process is named stimulated scattering. The evolution from spontaneous to stimulated scattering corresponds to a transition of the medium

behavior from a linear to a non-linear regime. Figure 1.1 shows a typical spontaneous scattering spectrum from solid state matter.

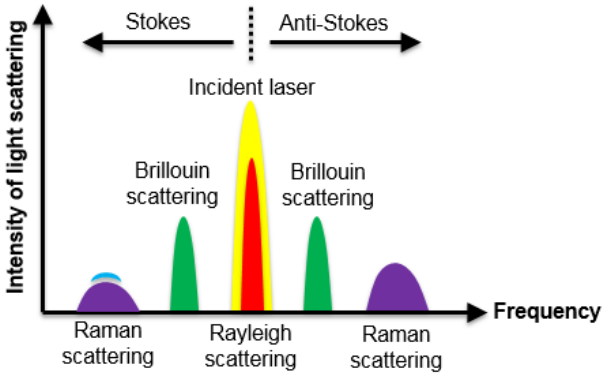

Figure 1.1 Light scattering spectrum

Optical time domain reflectometry (OTDR) profiling the intensity of Rayleigh backscattering along the length of an optical fiber was first introduced to monitor signal attenuation along an optical fiber to detect fault in telecommunication cables (Barnoski et al. 1977). It was then used to invent various novel fiber optic sensors for strain, temperature, and displacement monitoring with spatial resolution up to half a meter (Yilmaz and Karlik 2006, Pinto et al. 2006, Wan and Leung 2007). Polarization optical time domain reflectometry (POTDR) used a broadband frequency laser of ~0.1 nm to create a polarized pulse of light. The signal attenuation modulated with the local polarization state change is detected by Rayleigh backscattering. Polarization properties of an optical fiber can be modulated with various parameters such as pressure, strain, temperature, electrical and magnetic fields. However, the contributions of individual parameters are often difficult to separate (Rogers 1980, Hartog et al. 1980). Coherent OTDR (COTDR) means low coherent OTDR using coherent detection (Takada et al. 1991). Because the distances between scattering centers (particles) are smaller than the

wavelength of light in the optical fiber, the secondary light waves from Rayleigh scattering are coherent. Hence, the resulting intensity is the addition of the scattered fields. Coherent detection is realized by optical mixing of the backscattered light and reference light. With the balanced detection technique, the DC noise is reduced significantly, which gives a shot noise limited sensitivity of -140 dB at a 3 Hz bandwidth for millimeter spatial resolution when the sensing length is reduced to the distance in which the photon counting technique is introduced (Wegmuller et al. 2004). Phase OTDR utilizes a laser source with narrow spectral line width and low frequency shift to form the interference of Rayleigh backscattered signals whose amplitude can be modulated with vibration (Lu et al. 2010, Juarez et al. 2005, Qin et al. 2011). Phase OTDR means coherent light source with direct detection. In this case, a kHz line width laser is used with short pulses for coherent detection or large pulses for direct detection, where the spatial resolution of a few hundred meters can be achieved over with 12 km of fiber for intrusion sensing (Bao and Chen 2012). Accurate location information can be identified because of coherent Rayleigh scattering, unlike polarization OTDR, which can only be used as an alarm system to locate a starting point of fiber due to the continuous state of polarization (SOP) change in the optical fiber. Generally, the spatial resolutions of OTDR technologies are related to the pulse width in optical domain and thus the bandwidth of the detector, electrical amplifier and digitizer in electronic and digital domains. Millimeter spatial resolution measurement will require a bandwidth in the range of tens of GHz and will thus require a very expensive and sophisticated system (Bao and Chen 2011, 2012). Alternatively, optical frequency domain reflectometry (OFDR) can convert the frequency response into time domain via the Fourier transform so the spatial resolution with OFDR does not depend on bandwidth of the detector or digitizer (Kingsley and Davies 1985, Soller et al. 2005).

Brillouin scattering in an optical fiber describes the interaction of a light wave (photon) with an acoustic wave (phonon) that is equivalent to a characteristic density variation along the fiber, including spontaneous and stimulated Brillouin scatterings. Whether the Brillouin scattering is stimulated or spontaneous depends on whether the input light is scattered with strongly changing property of the medium (Bao and Chen 2011, 2012). The first demonstration of Brillouin scattering spectrum in a distributed fashion was based on stimulated Brillouin scattering (Horiguchi et al. 1989), namely Brillouin optical time domain analysis (BOTDA), which used pump and probe waves counter-propagating in an optical fiber. When the frequency difference between the pump pulse and probe continuous wave (CW) matches with the local Brillouin frequency, Brillouin gain or Brillouin loss will happen at that location. The Brillouin frequency shift can be modulated with strain and temperature changes (Brown and Hartog 2002, Belal et al. 2010). Distributed temperature measurement with 3°C temperature accuracy and a spatial resolution of 100m over a sensing length of 1.2 km was demonstrated (Culverhouse and Jackson 1989, Kurashima *et al.* 1990). Brillouin optical time domain reflectometry (BOTDR) was proposed with the advantage of monitoring the system from one end of a sensing fiber (Shimizu et al. 1993). Performance was improved by coherent detection with the total sensing length increased to 11 km with similar spatial resolution and temperature accuracy. However, the spatial resolution is around meter range, which is mainly limited by the pulse width. The key to achieving long distance fiber sensing is to limit the pump power so that low gain can be maintained over the entire sensing length, preventing gain saturation of the Stokes wave and reducing pump wave depletion. In addition to the power requirement, polarization state matching is also critical, as the choice of SOP for pump and probe waves should maintain modest gain over the entire sensing length, rather than high gain at the front of the fiber section. This is very

different from the condition of short sensing length, in which SOP matching is required to have as much gain as possible. On the fiber side, high stimulated Brillouin threshold fiber is preferred for long sensing lengths to ensure low Brillouin gain over the entire fiber (Bao et al. 1993, Bao et al. 1995).

Narrower bandwidth pulse can lead to higher resolution. However, it may not be able to stimulate sufficient acoustic waves. To generate significant stimulated Brillouin scattering, the pulse bandwidth must be longer than the phonon relaxation time. It has been demonstrated that 28 ns are required to get the phonon fully stimulated, which corresponds to 3 m spatial resolution. To solve this problem, pulse pre-pump Brillouin optical time domain analysis (PPP-BOTDA) was proposed to take advantage of a pre-pump pulse that stimulates the phonon before a narrow bandwidth pulse arrives and thus, a centimeter spatial resolution has been achieved (Kishida and Li 2006, Kishida et al. 2009, Kishida et al. 2012). At the same time, frequency domain distributed sensing technologies have been developed, such as Brillouin optical frequency domain analysis (BOFDA) (Garus et al. 1997, Golgolla and Krebber 2000) and Brillouin optical correlation domain analysis (BOCDA) (Hotate and Hasegawa 2000). For BOFDA, 3 cm spatial resolution has been realized over 9 m measurement distance (Bernini et al. 2012). For BOCDA, 1 cm spatial resolution has been reported over a short measurement distance (Hotate and Tanaka 2002) and 7 cm spatial resolution has been realized with 1 km measurement distance (Hotate 2011). With a differential Brillouin gain based on differential pulse-width pair (DPP-BOTDA) technology, the time-domain waveform is subtracted at the same scanned Brillouin frequency obtained from light pulses with different pulse widths, and the spatial resolution is appreciably improved to 2 cm with 2 km sensing length (Li et al. 2008, Hao et al. 2010, Dong et al. 2012).

In this study, PPP-BOTDA was used to measure the strain distribution in unbonded/bonded pavement overlays instrumented with distributed fiber optic sensors. To facilitate sensor installation, a cementitious mortar grid instrumented with distributed fiber optic sensors was prefabricated and then embedded in concrete overlay. Strain distributions were measured from the distributed sensors. In addition, numerical simulations were conducted to study the strain field in the unbonded pavement system.

Chapter 2 Experimental Study on Shrinkage-Induced Strains and Monitoring

2.1 Data Acquisition System

Neubrescope NBX-7020, as shown in figure 2.1, combines four independent distributed fiber optic sensing technologies and their hybrid modes. The four independent sensing technologies include pulse pre-pump Brillouin optical time domain analysis (PPP-BOTDA), Brillouin optical time domain reflectometry (BOTDR), tunable wavelength coherent optical time domain reflectometry (TW-COTDR), and coherent optical time domain reflectometry (COTDR). When the hybrid mode of PPP-BOTDA and TW-COTDR is applied, simultaneous strain and temperature measurements can be taken based on the different strain and temperature coefficients of Brillouin and Rayleigh scatterings. The measured distance can be up to 25 km. The readout resolution is up to 1cm, and the spatial resolution is up to 2 cm. The strain measurement ranges are -30,000 to +40,000 με (-3% to 4%) for PPP-BOTDA, and -15,000 to +20,000 με (-1.5% to +2%) for TW-COTDR. With strain-free ultraviolet (UV) coated optical fibers, measurement accuracies are 7.5 με / 0.35 ºC for PPP-BOTDA, and 0.5 με / 0.05 ºC for TW-COTDR. Their corresponding measurement repeatability is 5 με / 0.25 ºC for PPP-BOTDA and 0.2 με / 0.01 ºC for TW-COTDR.

Figure 2.1 Neubrescope NBX-7020

2.2 Load frame

A low capacity load frame (Instron 5965 with a capacity of 100 N) was used to test delicate optical fibers as shown in figure 2.2. It has up to 2.5 kHz data acquisition rate option simultaneous on load, extension, and strain channels with a displacement rate of 0.001~3000 mm/min (0.00004~120 in/min). It has automatic transducer recognition for load cell and extensometer. The load measurement accuracy is ±0.5% of reading down to 1/1000 of load cell capacity option (2580 series load cells).

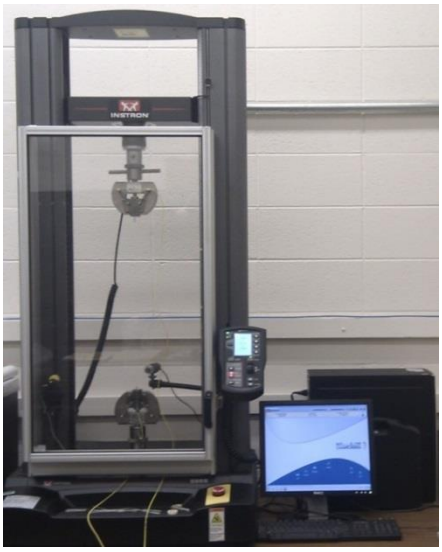

Figure 2.2 Load frame Instron 5965

2.3 Distributed Fiber Optic Sensor

Flexible optical fiber is made of high quality extruded silica glass, including a transparent core surrounded by transparent cladding. Typically, the refractive index of the core is higher than that of the cladding, thus forcing a total internal reflection (TIR) of travelling light at the interface of core and cladding. The light beam can be kept in the core, as shown in figure 2.3, namely waveguide. In terms of the propagation mode, both single mode fiber (SMF) and multi-

mode fiber (MMF) are widely used. A SMF is usually composed of 8.2-μm core and 125-μm cladding, as illustrated in figure 2.3. Considering its fragile nature, silica fiber is usually protected with a coating applied outside of the cladding.

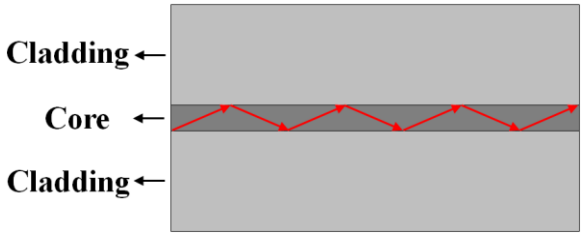

Figure 2.3 Schematic of TIR in a bare optical fiber

In this study, Corning SMF-28e$^+$ fiber is used as distributed fiber optic sensors. It is made of acrylics by UV curing. A dual-layer coating system is adopted. The glass is coated with an inner primary coating that is usually made of soft and rubbery material that cushions the glass from external mechanical impact loading. The inner primary coating is surrounded by an outer primary layer that is made of much stiffer material in order to protect the fiber from abrasion and environmental exposure. Both coatings are a mixture of raw materials (monomers, oligomers, photoinitiators, and additives). The cross section of BF is shown in figure 2.4. The inner and outer coatings are applied sequentially in a liquid form as the glass fiber is drawn. They are sequentially cured by exposure to UV light sources.

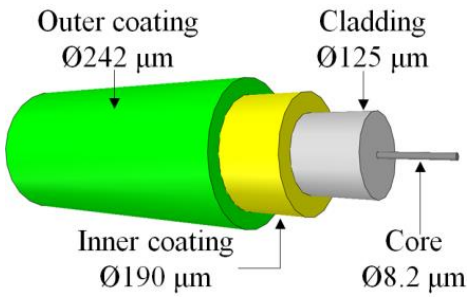

Figure 2.4 Structure of optical fiber with dual-layer coating

2.4 Characterization of Distributed Fiber Optic Sensors

2.4.1 Experimental Program

Each optical fiber was tested in uniaxial tension with a low capacity load frame at room temperature. Both mechanical and opto-mechanical tests were conducted as shown in figure 2.5.

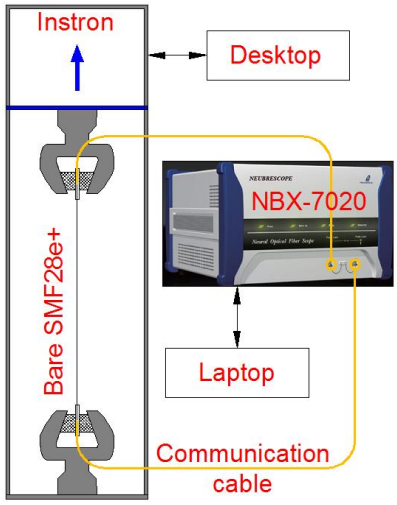

Figure 2.5 Tensile test setup

The mechanical tests were carried out to determine the mechanical property of optical fibers at room temperature (22°C), including the ultimate strength and the ultimate strain. Each fiber was tested to failure in displacement control with a loading rate of 2 mm/min. The loading force and extension were measured by embedded load transducer and extensometer in the load

frame, and recorded by the load frame. Given its initial length, each fiber was characterized with a force-strain relation from which the ultimate strength and the ultimate strain could be determined. With its fragile nature, each optical fiber was anchored with sufficient contact length to the load frame's grips, which was enhanced by protective sleeves. Each protective sleeve is composed of two polymer tubes with a steel bar in between. The optical fiber can be tightly gripped by the sleeve that could be in direct contact with the load frame.

The opto-mechanical tests were conducted with each optical fiber spliced with a communication cable and a FC/APC connector. Based on the estimated ultimate strain of a representative optical fiber, the increment of the loading process can be determined as appropriate. While the tensile strain in the optical fiber was incrementally increased and measured using the load frame, the distribution of the Brillouin frequency shift was simultaneously measured using the Neubrescope. At each increment, the strain measured from the load frame was correlated to the Brillouin frequency from the Neubrescope with PPP-BOTDA. Since the ambient temperature was kept constant, the Brillouin frequency shift was affected by the strain change only, from which the strain-frequency sensitivity coefficient can be determined.

2.4.2 Mechanical Properties

Ten optical fibers were tested to determine the mechanical properties. One of the measured force-strain relationships are shown in figure 2.6. The load linearly increased with the strain until the optical fiber ruptured. The tensile strength of the fiber was around 26 N and the corresponding strain was about 26,000 με (2.6%). The slope represents the fiber's tensile stiffness and can be obtained by linear regression. The slope was determined to be 9.63×10^{-4} N/με. The average tensile strength and strain capacity were determined to be 26 N and 2.6×10^{4}

με, respectively. In a previous study (Chen et al. 2014), the determination of mechanical properties was mentioned; however, the obtained tensile strength and strain capacity were not correct. The failure mode was rupture of coating and pull-out of glass fiber. The fibers were not ruptured, so the tensile strength and strain capacity were greatly underestimated.

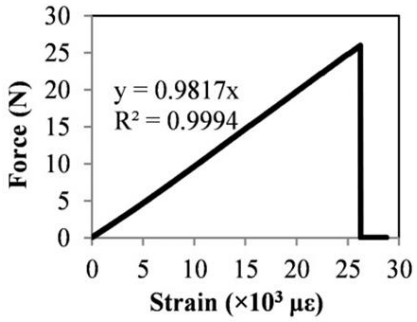

Figure 2.6 Force-strain relationship of optical fiber under tensile test

2.4.3 Strain Sensitivity Coefficient and Characteristics of PPP-BOTDA Measurement

The strain sensitivity and characteristics of PPP-BOTDA measurement have been introduced in the author's previous study. For convenience, the results are briefly introduced here. Figure 2.7 shows the Brillouin frequency shift associated with the strain obtained from the Instron. The slope represents the strain-frequency sensitivity coefficient, and can be determined to be 5.41×10^{-5} GHz/με by linear regression. The coefficient of determination was close to 1, indicating good correlation.

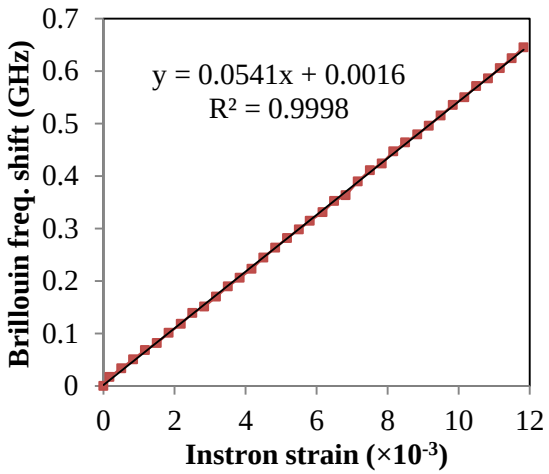

Figure 2.7 Calibration of optical fiber with PPP-BOTDA

In accordance with the comparisons of the strain measurements from both NBX-7020 and extensometer, the strain measurement accuracy of the bare SMF-28e$^+$ fiber was very good. For PPP-BOTDA measurements, the variations of strain measurement were very small.

For PPP-BOTDA, up to 1-cm readout resolution and 2-cm spatial resolution can be realized for UV coated SMF. Along the fiber one data point is collected every centimeter, and the strain values of any two points with a distance no less than 2 cm are expected to be distinguished.

2.6 Measurement of Shrinkage in Cementitious Mortar

One standard specimen was prepared and tested at room temperature (22±1°C) according to ASTM C1698. It was a 380 mm long corrugated cylinder with a groove diameter of 20 mm and a ridge diameter of 25 mm. As shown in Figure 2.8, the cylinder was cast in a 380 mm long corrugated polyethylene (transparent) mold with two 20 mm long specially shaped end plugs (20 mm in diameter). The plastic tube was retained, and the mortar was considered sealed and used to measure the autogenous shrinkage of a corrugated cylinder. The specimen was air cured at

60±3 % relative humidity and 22±1°C temperature. The initial and final setting times were determined by the Vicat Needle test according to ASTM C191.

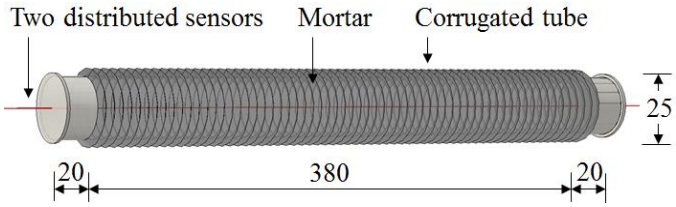

Figure 2.8 Illustration of the sealed specimen (unit: mm)

The mortar tested in this study corresponds to an ultra-high-performance mixture that exhibits high autogenous shrinkage at early age. The water/cementitious material/sand mixture design of the mortar was set to be 0.2/1.0/1.0 by weight. The cementitious material consists of 40% Type III cement and 60% Class C fly ash by volume. To improve the workability, superplasticizer dosage corresponding to 1.2% of the cementitious material was added.

The specimen was instrumented with two distributed optical fiber sensors that were closely deployed approximately 1 mm inside the specimen surface at grooves. One sensor was directly bonded to the mortar to measure the combined effect of strain and temperature. The other sensor was placed inside a 450 mm long steel tube with inside and outside diameters of 0.5 and 1.0 mm, respectively, in order to measure temperature only, which was used to separate the temperature from the combined strain and temperature effect in the first measurement. To simplify the measurement process, two sensors in each specimen were connected in series so that one measurement was sufficient to evaluate both temperature and strain along the length of the optical fiber (Bao et al. 2015).

To protect the two optical fiber sensors from damage during mortar casting, they were placed inside a 450 mm long aluminum tube with inside and outside diameters of 3 and 4 mm,

respectively, as illustrated in figure 3(a). Prior to mortar casting, the aluminum tube was passed through a 5 mm-diameter hole drilled on each end plug of the corrugated mold. After approximately 5 minutes of mortar casting, the aluminum tube was removed, leaving the optical fiber sensor used for strain and temperature measurements, and the steel tube with the second optical fiber sensor for temperature compensation in direct contact with the freshly cast mortar. This process proved efficient to embed the optical fiber sensors. No air pockets can be observed near the sensor, as shown in figure 2.9.

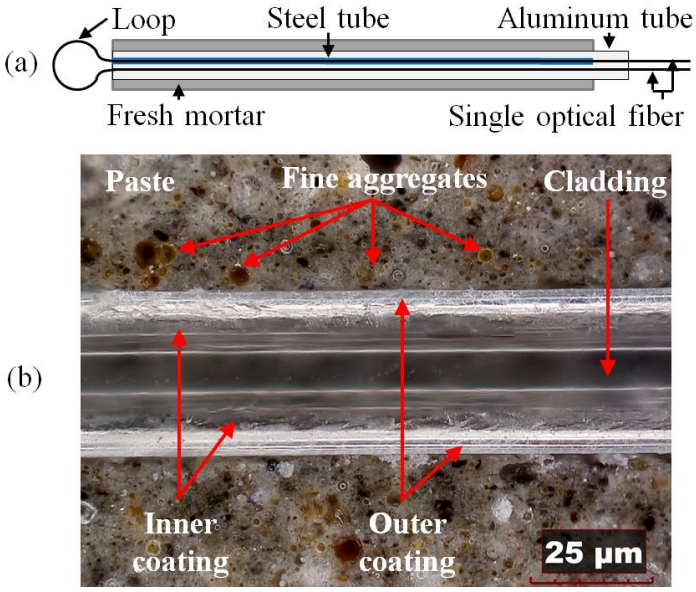

Figure 2.9 Preparation and microstructure of the specimen instrumented with optical fiber sensor: (a) illustration of the preparation, and (b) longitudinal profile of the specimen

It was observed during casting that the mortar with 0.2 w/cm ratio was easy to flow yet stable to prevent potential segregation of the mortar ingredients. This property was desirable for installation of the optical fiber sensor following the proposed procedure. The initial and final setting times determined by the Vicat Needle test were 75 and 300 min, respectively.

At various curing times up to 14 days after the final setting, the SBS along the length of each optical fiber was measured by a commercial Neubrescope (Model: NBX-7020). As indicated in equation 1, the Brillouin frequency shift due to strain effect alone was evaluated by subtracting the temperature-induced frequency shift from that of the distributed optical fiber sensor as a result of combined strain and temperature effect. For comparison and validation, the ASTM standard test for shrinkage measurement was conducted at corresponding curing times.

Figure 2.10 shows the strain distribution along the embedded optical fiber in the mortar specimen after 1, 3, 7, and 14 days of curing after final setting. The horizontal axis represents the distance of optical fiber measured from its connection to the measurement instrument (Neubrescope). The portion of optical fiber in direct contact with mortar is specified in figure 2.10. The strain measured along the length of the mortar specimen was negative and not uniform, indicating non-uniform compressive strain due to shrinkage. For convenience in the following discussion, shrinkage strain (positive) is referred to the absolute value of the measured strain (negative). Shrinkage strain values at 2.87-2.99 m along the fiber length are consistently larger than those at 3.03-3.23 m; the minimum value occurred at 2.99-3.03 m as marked between the two vertical lines, where a shrinkage induced crack was observed on the surface of the test specimen. Each strain peak corresponded to the location of the crack. The release of shrinkage strain near the crack was small and slightly increased over time; the crack affected zones bounded by the two vertical lines at various curing ages were nearly identical. Both observations from figure 2.10 indicated that the crack was small and slightly widening over time and the optical fiber remained perfectly bonded to the mortar.

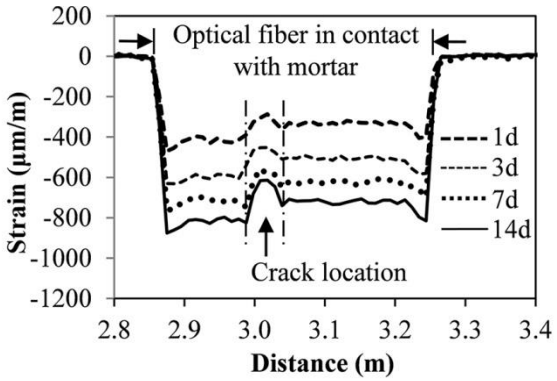

Figure 2.10 Strain distribution measured by optical fiber sensors

Figure 2.11 compares the proposed method with the ASTM standard test. The average value of each strain distribution is in agreement with the corresponding strain measured by ASTM C1698. The ASTM method gives the average shrinkage strain of the specimen by dividing the directly measured shrinkage deformation between the two ends of a specimen by the specimen length. Therefore, the ASTM method cannot be applied to investigate the non-uniform shrinkage behavior over the specimen length. Each error bar in figure 2.11 represents the maximum and minimum strain values of various strain distributions at different curing ages. The maximum value corresponds to the peak of each strain distribution shown in figure 2.10. The shrinkage strain increased rapidly at the beginning of curing and became stabilized after approximately seven days.

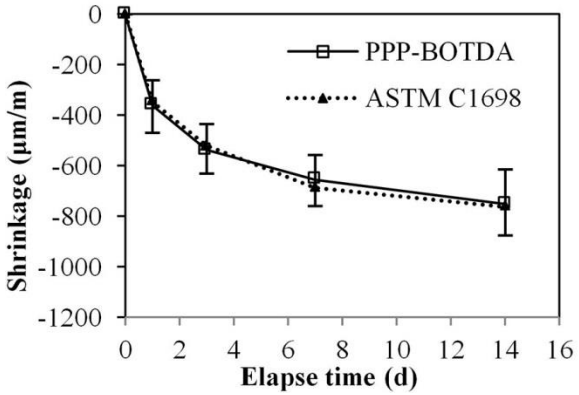

Figure 2.11 Comparison of the ASTM standard test and the proposed method

Based on the experimental results, early age autogenous shrinkage strain in cement-based materials is not uniform. It can be measured from the proposed optical fiber sensor. The average value of distributed strain is in agreement with that determined using the ASTM standard method. A shrinkage-induced crack can be visually identified from the strain distribution measured from the optical fiber sensor so long as it intercepts the optical fiber. The location of a crack is represented by its corresponding strain peak. The width of the crack is closely related to the magnitude of the strain peak.

2.7 Summary

Strain sensitivity coefficient of the distributed fiber optic sensor was experimentally calibrated to be 0.0541 MHz/με. The optical fiber's mechanical performance was evaluated. The tensile force capacity is about 26 N, and strain limit is about 26,000 με (2.6%).

The distributed sensor was successfully used to measure autogenous shrinkage in cementitious mortar. The measurement was in agreement with the ASTM standard method. Non-uniform shrinkage was detected by the distributed sensor, and crack was identified from the strain distribution.

Chapter 3 Fabrication of Smart Grid

3.1 Concept of the Smart Grid

Considering the optical fiber's fragility to shear force, its operation in real practice needs extra attention to ensure its survival during construction. An installation method applicable for field practice was proposed and implemented in the authors' previous study (Chen et al. 2014). A thin mortar layer was cast in-situ to encapsulate the optical fiber and thus provided mechanical protection. However, while applicable, it is time-consuming to cast mortar in the field and repair the optical fiber damaged during installation or mortar casting.

In this study, mortar grid instrumented with distributed fiber optic sensors, namely smart grid, was designed and implemented in the field. Figure 3.1 illustrates the smart grid. An optical fiber is continuously deployed in the mortar grid. The optical fiber forms a loop for light signals passing through. The thick lines (in green) represent the fiber portions isolated from strain or deformation change, for temperature compensation. Two-dimensional strain distributions can be measured and mapped using the smart grid. In addition, multiple cracks can be detected from the measured strain distributions (Chen et al. 2014). Cracks can be represented by sharp strain peaks and located at positions of the peaks (Bao et al. 2015).

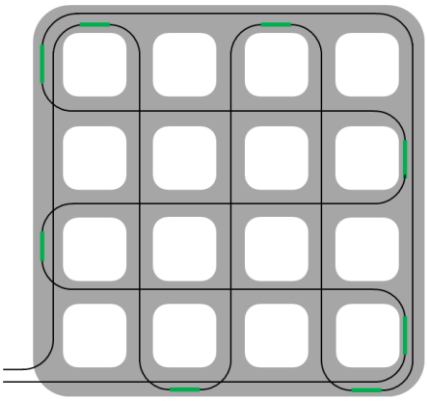

Figure 3.1 Smart grid – a prefabricated mortar frame with one embedded distributed fiber optic sensor

The smart grid can be prefabricated in a plant at a high quality, placed on existing pavement, and cast over with fresh concrete to complete a concrete overlay with an embedded sensor. It can potentially be implemented in reinforced concrete structures such as buildings, bridges, and tunnels. For example, a smart grid can be installed in the bridge deck or floor slab in buildings to provide strain and temperature measurements. The smart grid can be made of common cementitious mortar and telecom optical fiber, both inexpensive. Therefore, it is a cost-effective solution to the monitoring of pavement.

3.2 Preparation of Distributed Fiber Optic Sensor

Typically each distributed fiber optic sensor consists of sensor portion, transmission cable, and connector to a data acquisition system, as illustrated in figure 3.2. In theory, the sensor portion and the transmission cable could be the same. In practice, however, they may have different packaging structures depending on specific applications. For example, the transmission cable is usually packaged with multiple layers of protective coating and sheath in order to ensure its survivability under brutal actions at construction sites. The sensor portion may be covered for mechanical protection when used for temperature measurement, but not be protected with loose sheath for strain measurement to ensure its accuracy and sensitivity. In the case that the strain sensor portion must be coated for minimum protection, strain transfer through the coating must be taken into account.

Different types of optical fibers can be connected in series to fit a specific need in application. For instance, when two distributed sensors are used to monitor two separate areas, they can be connected with a transmission cable. When the temperature change is insignificant, the transmission cable that is isolated from strain or deformation effect can serve as a distributed temperature sensor and provide temperature compensation for its adjacent strain sensors.

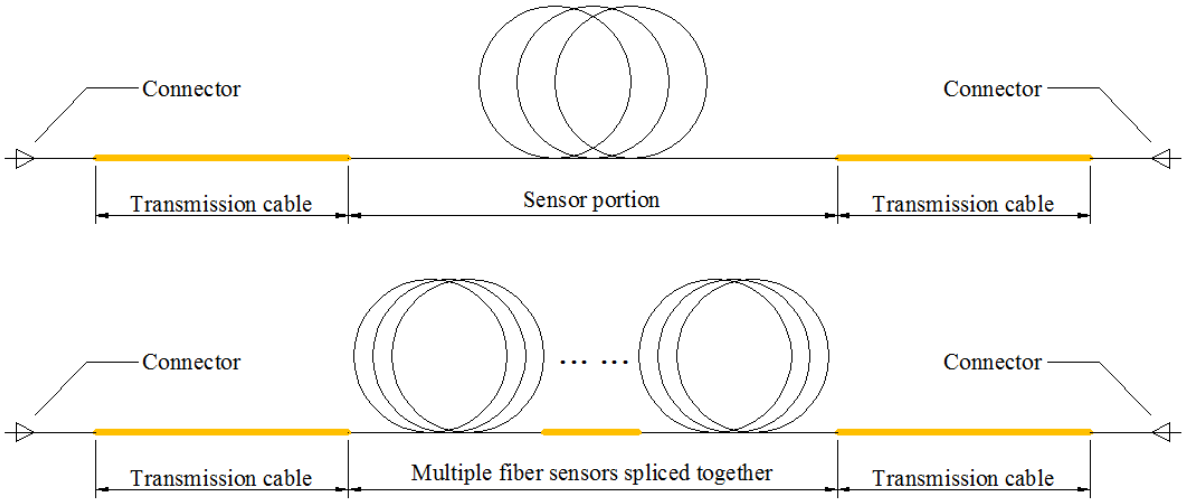

Figure 3.2 Structure of distributed fiber optic sensor

Multiple optical fibers can be spliced into one for overall measurement using the fusion splicing technique. The splice loss was controlled within 0.02 dB. Figure 3.2 shows a fusion splicer. To perform fusion splicing the protective coating needs to be removed, and the optical fiber will become fragile without the coating. To ensure that the fiber survives this action, sleeves are used to protect the splicing points.

Figure 3.3 Fusion splicer

3.3 Fabrication of the Smart Grid

Based on the designed dimensions of a smart grid, polyvinyl chloride (PVC) formwork

was fabricated. Thin plastic film was laid at the bottom of the PVC formwork, and cementitious mortar was cast on top of the plastic film. Optical fibers were embedded in the mortar near the top surface. In this study, for simplicity, optical fibers were only deployed in one direction, as shown in figure 3.4. To avoid shrinkage cracking, the specimen was wet cured. Due to the plastic film in between, the mortar specimen could be easily demolded from the PVC formwork after one day of curing.

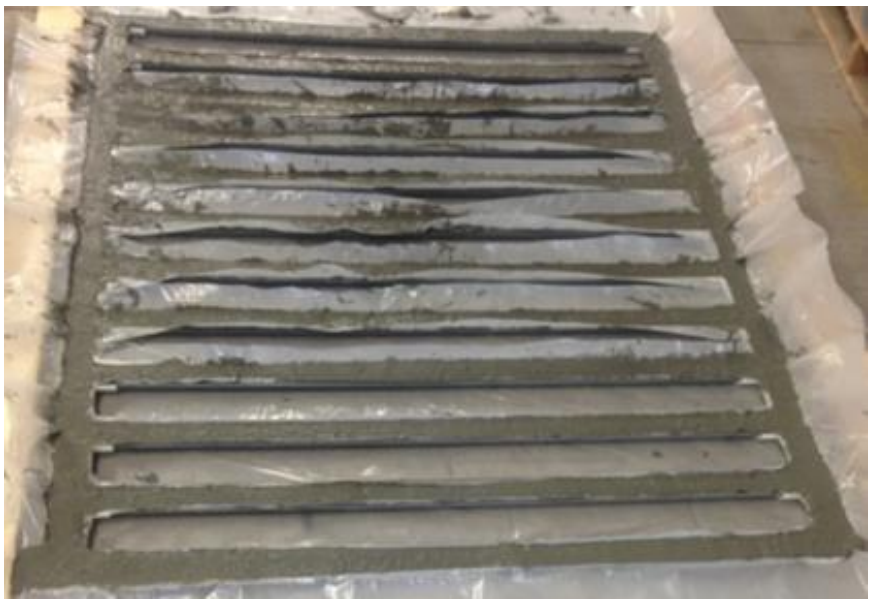

Figure 3.4 Fabrication of smart grid

Figure 3.5 A smart grid laid on top of fabric sheet

3.4 Instrumentation of the Smart Grid

Figure 3.6 illustrates the deployment of optical fiber in the smart grid specimen. The optical fiber was passed through the PVC formwork in a serpentine fashion to maximize the covered area. Since the optical fiber was in direct contact with the mortar (host matrix), the fiber was able to sense both strain and temperature changes. To compensate the temperature change, two lengths were passed through polymer sleeves, as indicated by solid yellow lines, to isolate the strain change. In each specimen, two distributed sensors were deployed. The two sensors were closely spaced and parallel to each other.

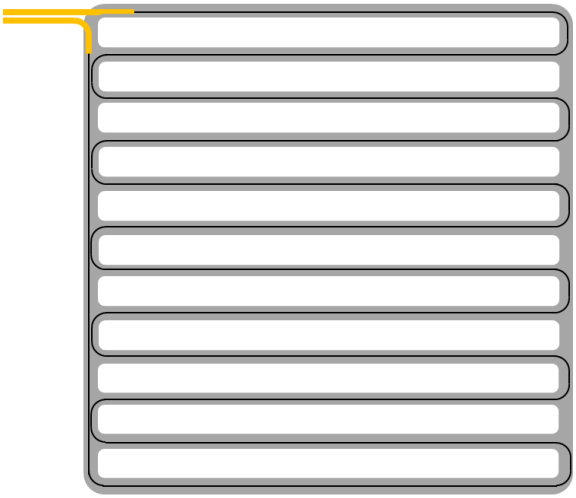

Figure 3.6 Instrumentation of smart grid

3.5 Materials

Materials and mix design used in this study are listed in Tables 3.1 and 3.2, respectively. Micro synthetic fiber (Fibermesh 650) was uniformly mixed into concrete as secondary reinforcement. Local aggregates were used, but the sizes and properties were in accordance with the proposed design.

Table 3.1 Materials

Aggregates					
	Pit No.	*Pit Name*	*Size*	*Absorption*	*Gravity*
Coarse aggregate	71041	Elk River	#67	0.013	2.69
Fine aggregate	71041	Elk River	Sand	0.009	2.63
Cementitious and Admixtures					
	Manufacturer/Supplier		*Admix Name*	*Class*	*Gravity*
Cement	Holcim-St. Genevieve		STGBLMO	I/II	3.15
Fly ash	Headwaters-Coal Creek		COVUNND	C/F	2.50
Admix #1	Sika AE260		-	AEA	-
Admix #2	SikaPlastocrete 161		SIPC161	A	-
Admix #3	SikaSikament 686		SIKA686	A	-
Admix #4	SikaViscocrete 2100		SIVIS2100	F	-

Table 3.2 Mix design

MNDOT mix number	**MR3A21-2F**	
Water	228	
Cement	420	70%
Fly ash	180	30%
Total cementitious	600	Agg.
w/cm Ratio	0.38	proportions
Sand	1235	41%
Coarse aggregate #67	1790	59%
Air content	7%	
Slump range	1” ~ 4”	
Admix #1 dosage range	-	
Admix #2 dosage range	0-5	oz/100# CM
Admix #3 dosage range	0-12	oz/100# CM
Admix #4 dosage range	0-6	oz/100# CM
Volume (27 ± 0.1 cf)	27.20	
Theoretical unit wt. (lb/cf)	142.6	

Chapter 4 Full-Scale Field Implementation

4.1 Construction

The proposed distributed fiber optic sensing technology and FBG sensors have been implemented in Minnesota's Cold Weather Road Research Facility (MnROAD). The layout, test, and instrumentation of the MnROAD facility parallel to I-94 are briefly introduced in figure 4.1. The specific site tested is labelled as Cell 40 in figure 4.1.

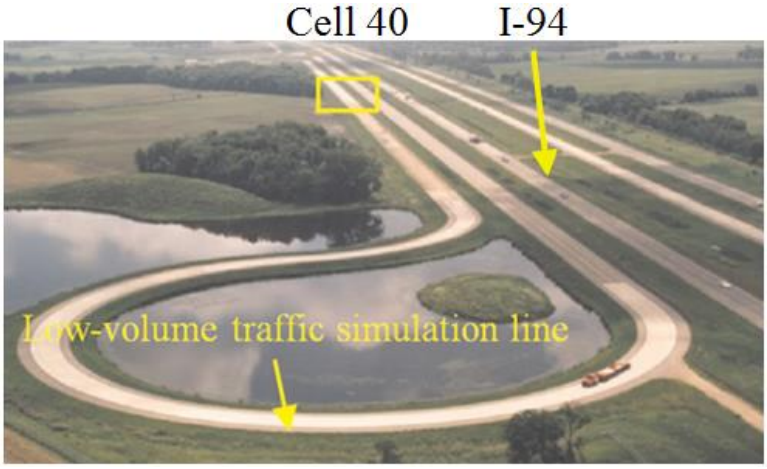

Figure 4.1 Minnesota's Cold Weather Road Research Facility (MnROAD)

To construct unbonded pavement overlay, a 3-mm fabric sheet was smoothly laid on top of the existing pavement, covered with 75-mm thick concrete overlay, and then cut into 1.83 m × 1.83 m panels after wet curing for 28 days. Concrete pouring was performed using a slipform paver. The fabricated grid with optical fiber sensors was laid on top of the fabric sheet before the fabric sheet was covered with concrete overlay, as shown in figure 4.2.

During concrete casting, the grid specimen could be disturbed by lateral force induced by asymmetric flow of concrete. To prevent potential movement, two pairs of rebar cage were used to anchor the grid. For the transmission cable that was not embedded in the grid specimen, two

failure modes may occur: rupture due to either tensile or shear force and macro-bending with acute angle. Macro-bending with a small radius causes significant signal loss, which can be detected as a fault equivalent to a break point. To protect it from failure during construction, the transmission cable was passed through a hose embedded underground. The length that was neither embedded in the grid specimen nor protected by the hose was attached to the fabric sheet using tape to avoid potential damage.

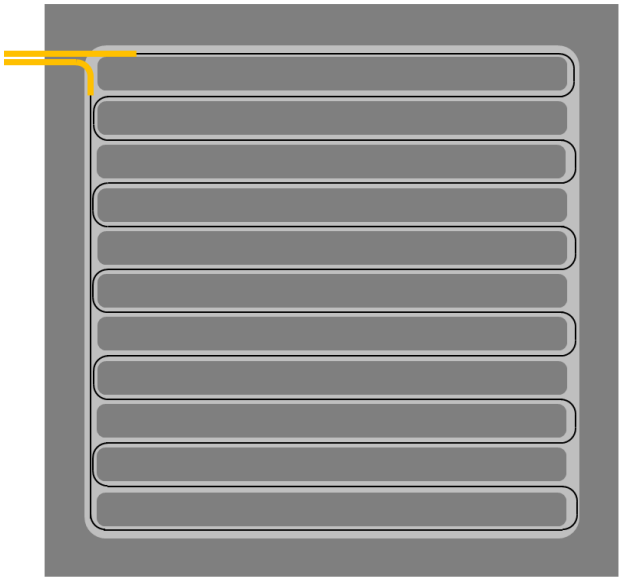

Figure 4.2 *In-situ* construction of unbonded pavement instrumented with smart grid

4.2 Vehicle Loading Test Scenario

The pavement panels were loaded using a fully-loaded truck. The loading scenario is shown in figure 4.3. At each loading position, Brillouin frequency shifts were measured from the distributed sensor using the Neubrescope. The strain distributions could thus be obtained by converting the frequency shift into strain change, using the strain-frequency sensitivity coefficient determined in chapter 2.

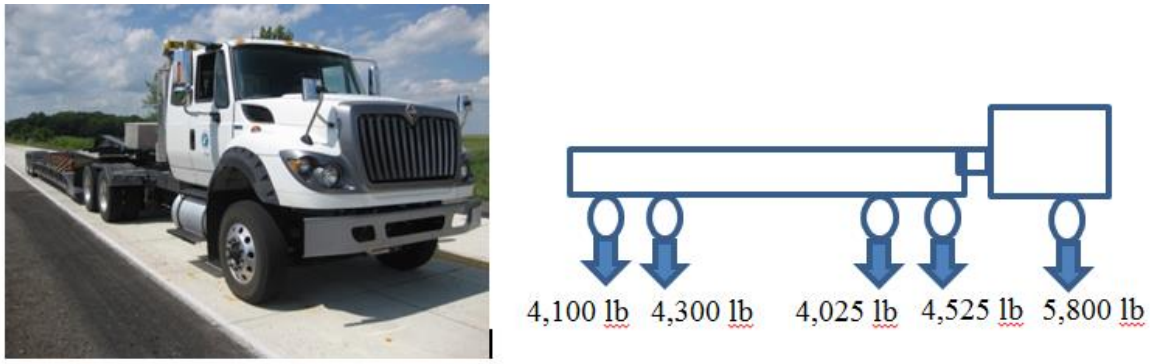

Figure 4.3 Load distribution of the vehicle

The position of the test vehicle was measured with a measuring tape, as illustrated in figure 4.4. The center of the contact area between the tire and the pavement was precisely located and correlated with the location of the optical fiber. The longitudinal direction along the driving direction was represented by *x* and the transverse direction was *y*.

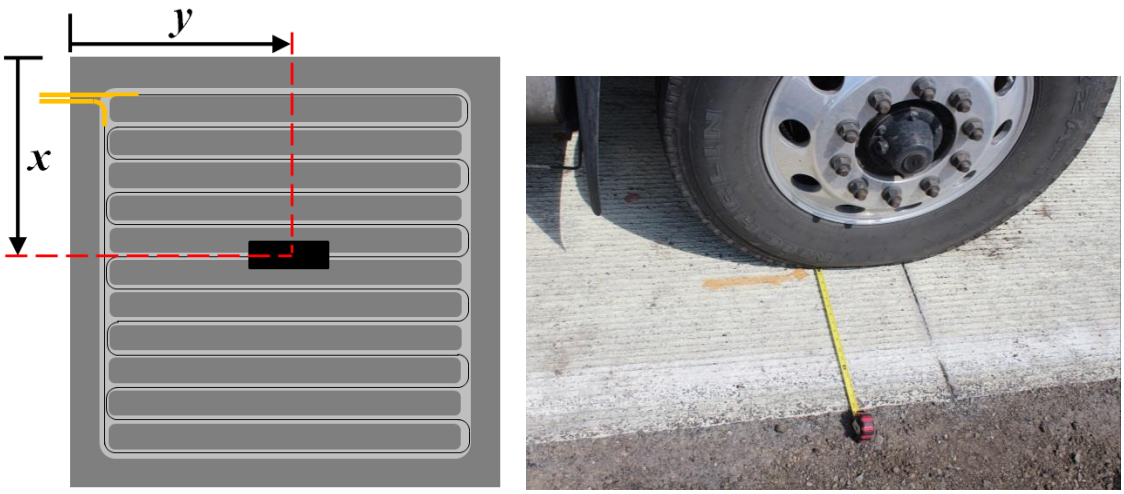

Figure 4.4 Position of the vehicle tire

The contact area usually depends on the inflation of tires, the total weight, and the mass distribution of the truck. It increases with the decrease of the inflation pressure and with the increase of the truck weight. Typically, the width of the contact area does not significantly

change since the width of the tire is fixed. The inflation pressure was 90 ~ 100 psi for each tire of the vehicle. The contact area between the overlay and substrate was approximately 12×20 cm^2.

4.3 Test Results and Discussion

When loaded repeatedly by the truck, the overlay experienced a crack, as illustrated in Figure 4.5. With a measurement tape, the location of the crack was determined and correlated with the distributed fiber optic sensors, as shown in figure 4.5. The crack passed through the distributed sensors. The intersections were marked by circles and named as "C1-1," "C1-2," "C1-3," and "C1-4."

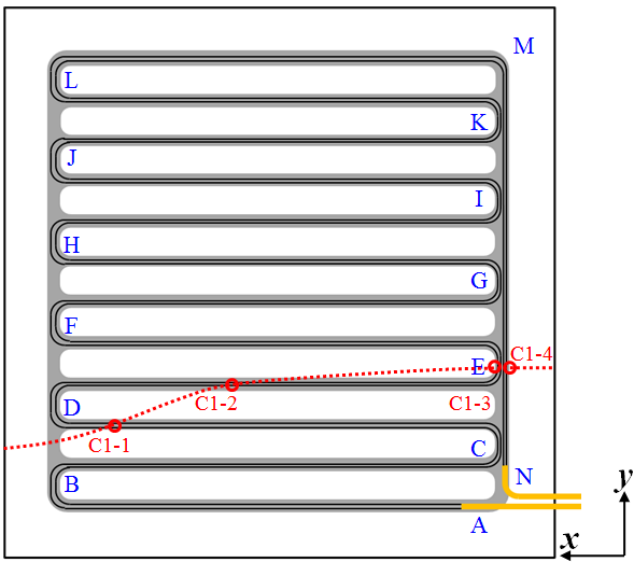

Figure 4.5 Relative position of the transverse crack and the distributed sensors

Figure 4.6 shows the measured strain distributions from the two closely-spaced distributed sensors. The strain distributions from the two sensors were in good agreement. The crack can be identified from the strain distributions as sharp peaks.

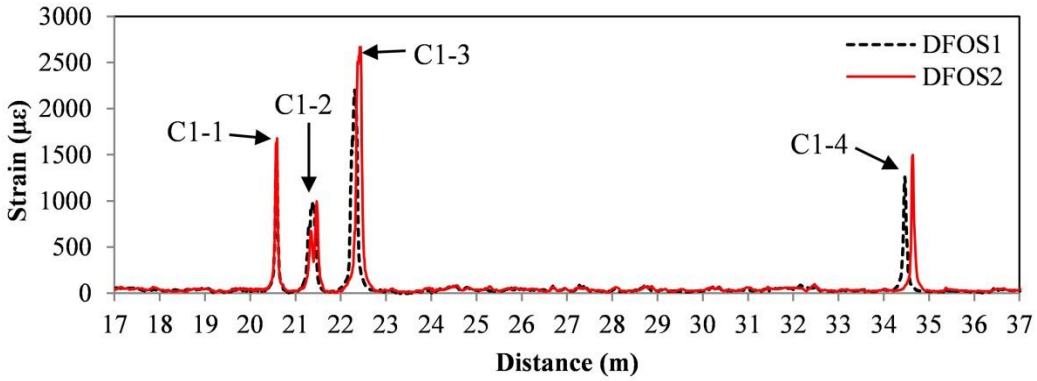

Figure 4.6 Relative position of the transverse crack and distributed sensors

4.4 Summary

The distributed fiber optic sensor was successfully implemented in the Minnesota's Cold Weather Road Research Facility (MnROAD). Unbonded pavement overlay was instrumented with distributed sensors. The overlay was repeatedly loaded using a truck. Crack in the overlay was successfully detected by the distributed sensors.

Chapter 5 Numerical Simulations

5.1 Modelling

Numerical simulations were carried out with the software ABAQUS to further understand the behaviour of the *in-situ* unbonded pavement overlays under truck loading. Since the overlay panels instrumented were identical in theory, only one panel was selected, as illustrated in figure 5.1. The dashed lines in figure 5.1 represent the cut lines between adjacent panels. The longitudinal and transverse directions of the pavement overlay are defined as *x*-axis and *y*-axis, respectively. The point line represents the rest of the test truck that includes another two axles. According to figure 4.3, Axle 1 and Axle 2 represent the heaviest single and double wheels, respectively. Axle 1 corresponds to 2 wheels, and Axle 2 corresponds to four wheels.

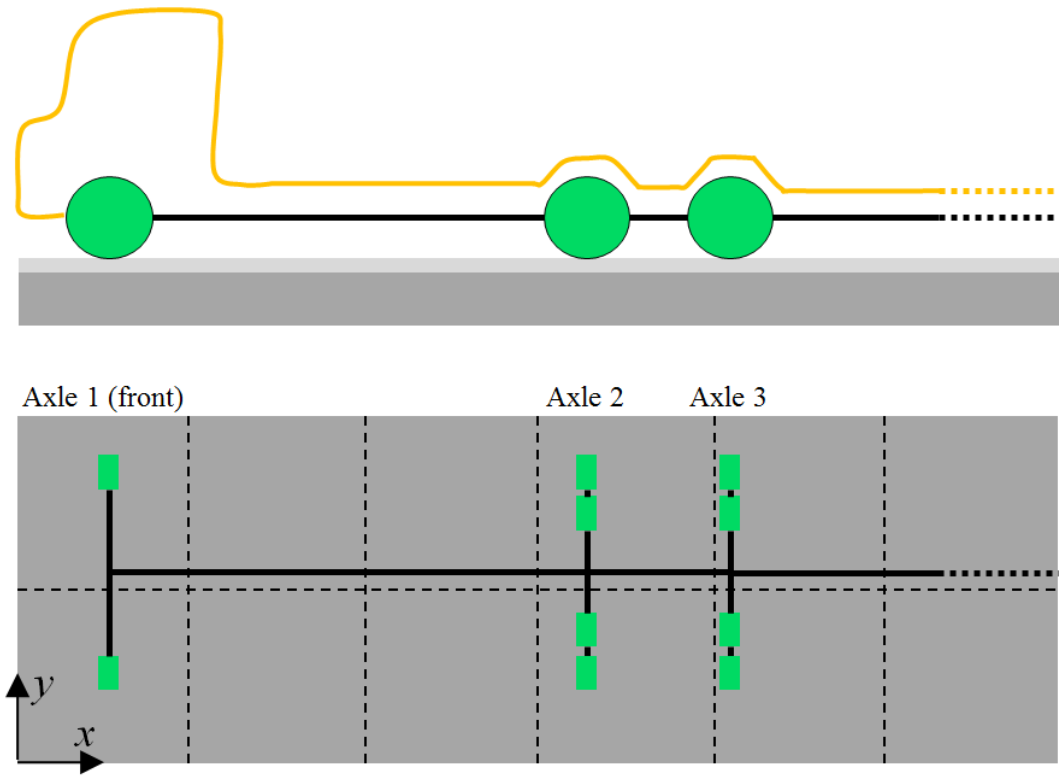

Figure 5.1 *In-situ* layout of unbonded pavement overlays

A three-dimensional finite element model was established with the consideration of nonlinear contact between the substrate concrete and the overlay, as shown in figure 5.2. The axis z represents the vertical direction (downward). Since the overlay is not mechanically bonded to its substrate, the interface can transfer compression, but not tension in vertical direction. Under external loads, the overlay can potentially be separated from the substrate.

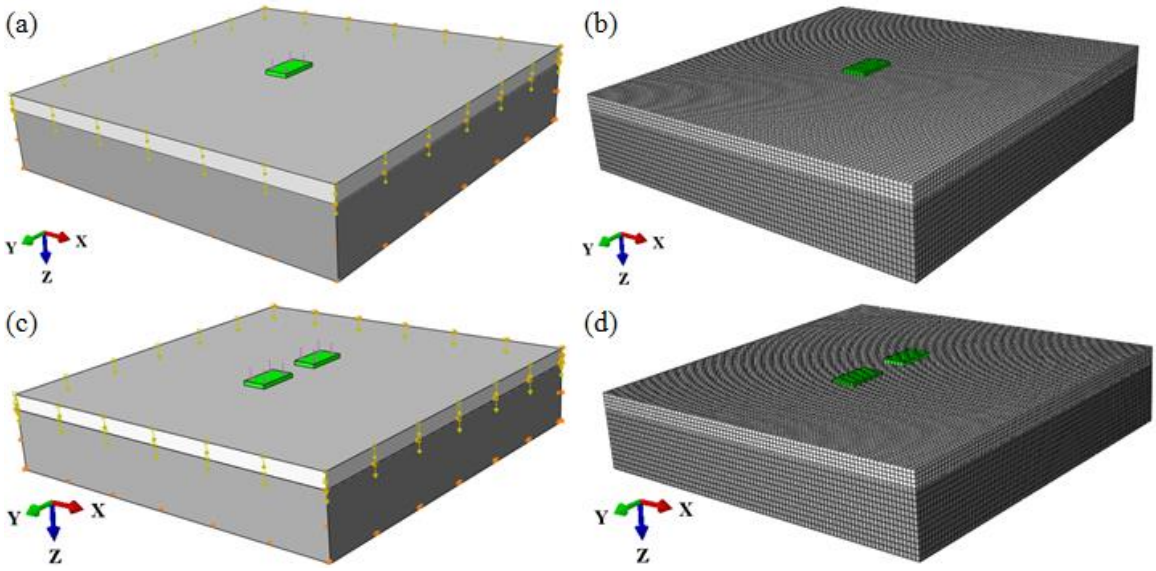

Figure 5.2 Finite element model of the pavement: (a) single wheel load and boundary conditions, (b) meshing with a single wheel load, (c) double wheel load and boundary conditions, and (d) meshing with a double wheel load

The axle loads are transferred through tires that are in direct contact with the overlay. Thus, the wheel loads can be simulated using pressure on tires. Strictly speaking, the pressure is not uniform over the tire and its distribution varies with many parameters, such as the type and inflation pressure of the tire. However, the range in pressure distribution is expected to change little of the strain distribution in the pavement. Hence, for simplicity, the pressure is considered

to be uniform in this study. The contact area was measured to be 12×20 cm^2. According to figure 4.3, the contact pressures corresponding to Axles 1 and 2 were taken be 0.53 and 0.21 MPa, respectively.

For material properties, the concrete substrate and overlay have a density of 2500 kg/m^3, the Young's modulus of 2.6 GPa, and a Poisson's ratio of 0.25. The rubber tire has the Young's modulus of 10 MPa, and the Poisson's ratio of 0.49. The element type used in this model was C3D8R in ABAQUS, an 8-node linear brick element with reduced integration. The meshing size was 2 cm. The entire model has 67,000 elements.

5.2 Loads

Four load cases, illustrated in figure 5.3, were investigated to combine two loading positions and two types of wheel: single-wheel load at center and edge, and double-wheel load at center and edge. The single-wheel load corresponds to Axle 1, which is the front axle. The double-wheel load corresponds to Axle 2, which is the heaviest rear axle.

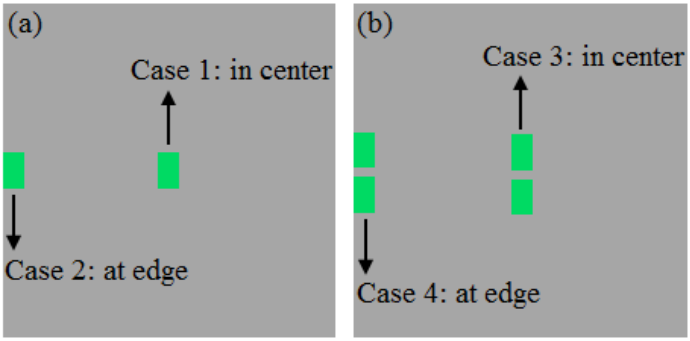

Figure 5.3 Load cases with single- and double-wheels at center and edge

5.3 Simulation Results and Discussion

5.3.1 Single-Wheel Load at Center

Figures 5.4(a) through (d) show the normal stress in overlay concrete when subjected to a

single-wheel load at center of the overlay. The bottom center zone is in tension with the maximum tensile stress of approximately 0.17 MPa, which is 32% of the applied tire pressure (0.53 MPa).

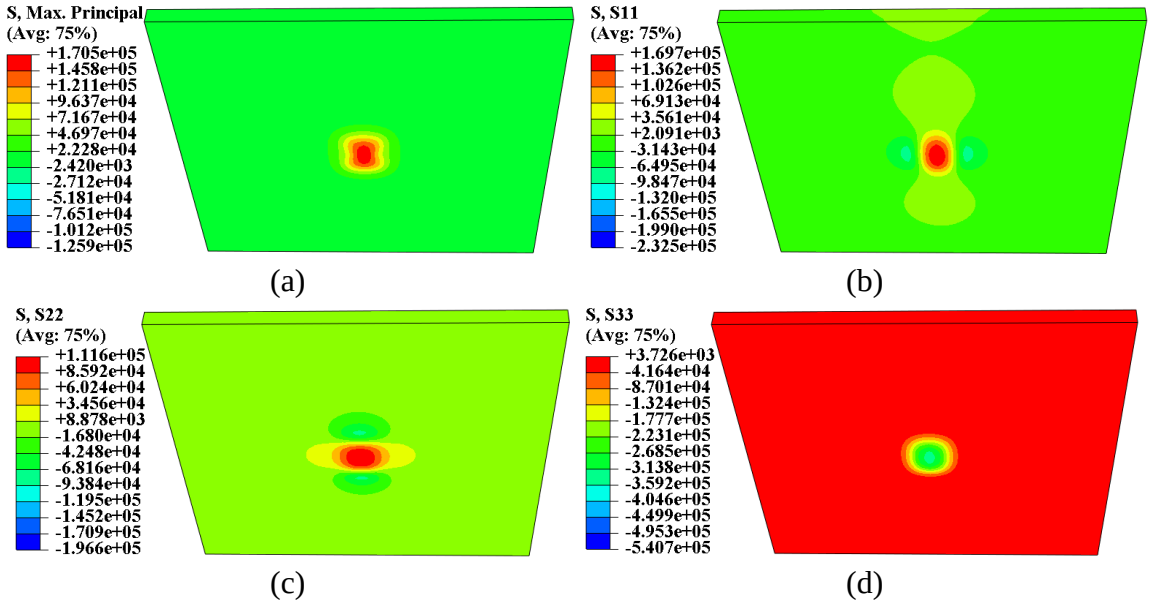

Figure 5.4 Normal stress at contact face (bottom) of overlay: (a) maximum principal, (b) longitudinal, (c) transverse, and (d) vertical

Figures 5.5(a) to (d) present the corresponding normal strains at contact face or bottom of the concrete overlay. The bottom center zone is in tension, which is consistent with the stress distribution shown in figure 5.4. The maximum tensile strain is approximately 89 με. Near the tensile zone are two compression strain zones in the longitudinal and transverse directions, respectively. The maximum compressive strain in each direction is approximately one half of the corresponding tensile strain. For example, as shown in figure 5.5(b), the maximum tensile strain is 88 με and the maximum compressive strain is 44 με.

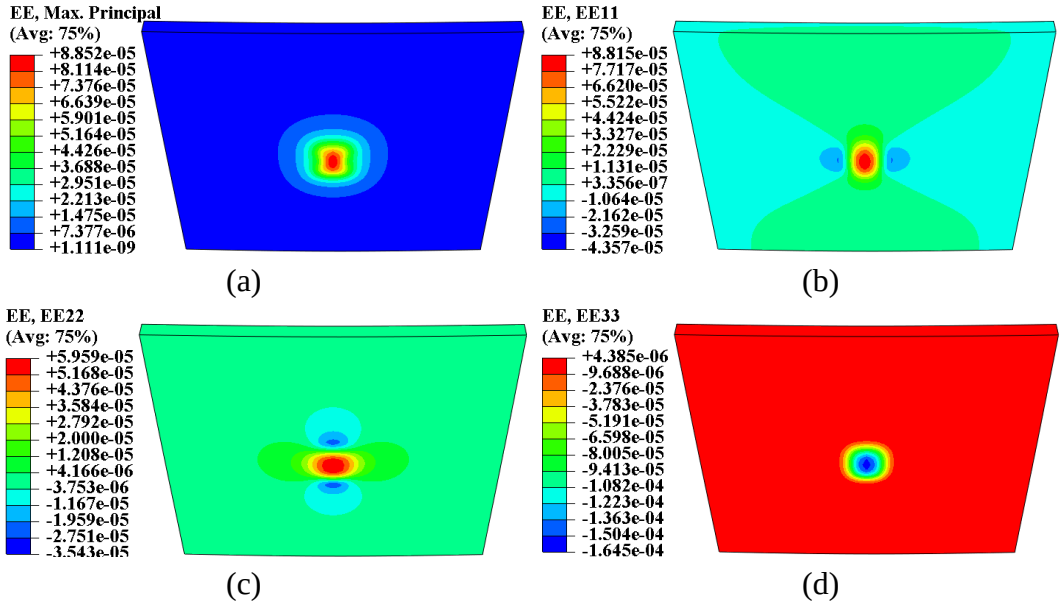

Figure 5.5 Normal strain at contact face (bottom) of overlay: (a) maximum principal, (b) longitudinal, (c) transverse, and (d) vertical

Figures 5.6(a) and (b) respectively show the contact status and the opening width between the overlay and its substrate. As shown in Figure 5.6(a), the overlay is not in direct contact with the substrate near to the center of overlay (in blue). Potential separation at the interface face is due to the effect of wheel load. As illustrated in Figures 5.7(a) and (b), the wheel load results in a concave upward deformation around the loading tire. Without the self-weight of overlay, the areas other than the localized contacting area are separated from the substrate, as indicated in figure 5.8. However, the self-weight of overlay can counteract the bending effect of wheel load, as illustrated in figure 5.7(b).

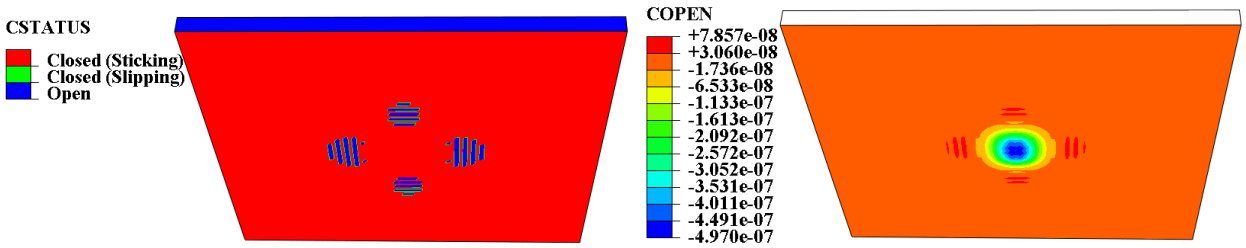

Figure 5.6 Contact behavior under combined wheel load and concrete weight: (a) contact status, and (b) opening width

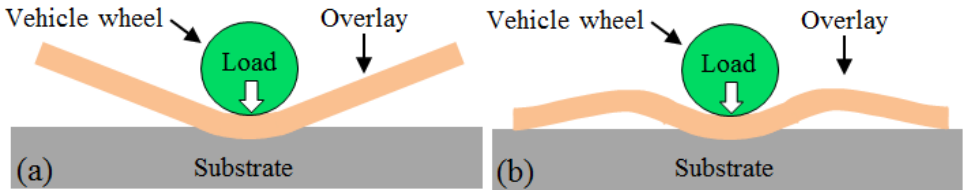

Figure 5.7 Separation mechanism of unbonded overlay (not in scale): (a) under wheel load alone, (b) under combined wheel load and self-weight

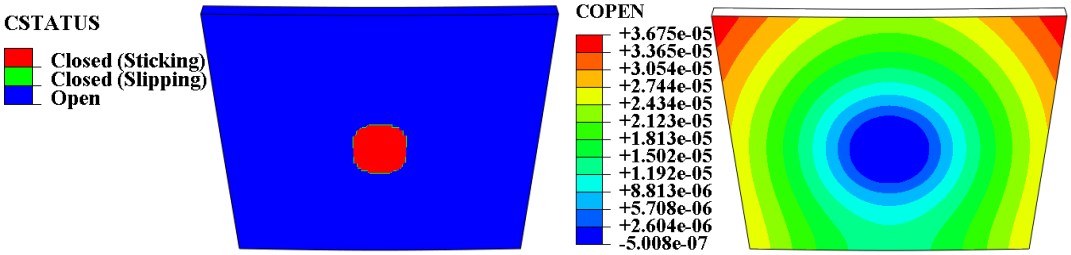

Figure 5.8 Contact behavior in the vertical direction of overlay under wheel load alone: (a) contact status, and (b) opening distance

The opening causes a non-uniform distribution of contact pressure, as shown in figure 5.9. The non-uniform distribution gives a higher maximum contact pressure. With a 0.53-MPa tire pressure applied, the maximum contact pressure is 0.32 MPa, which is about 61% of the applied stress. This reduction is due to the load distribution via the overlay concrete.

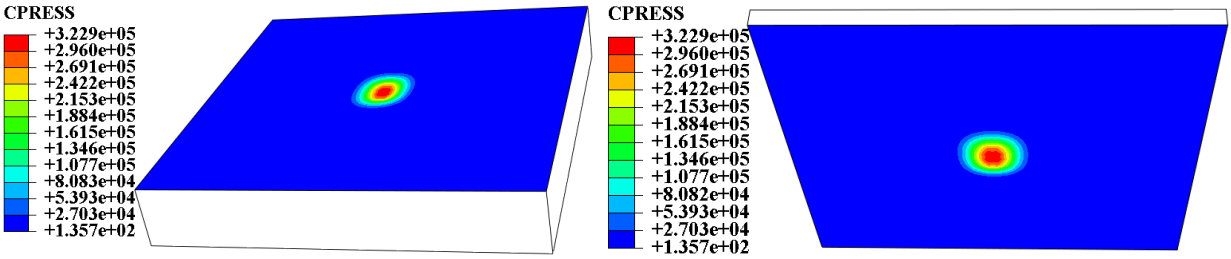

(a) (b)

Figure 5.9 Contact pressure: (a) in the substrate, and (b) in the overlay

Figures 5.10(a) and (b) show the shear stress distribution at the contact surface, which results from the friction at the contact faces.

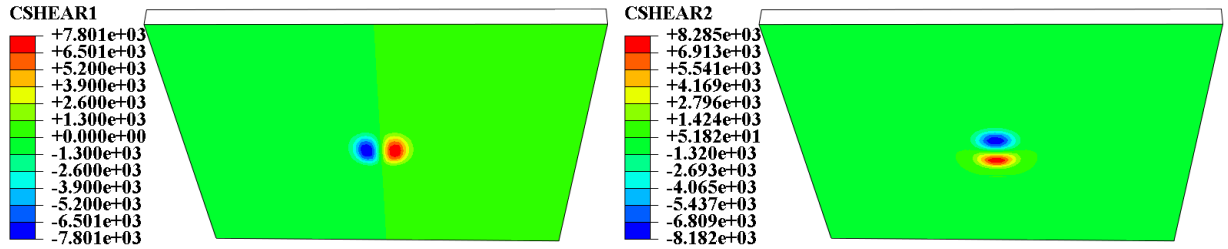

(a) (b)

Figure 5.10 Shear stress distribution at contact face (bottom) of substrate: (a) in the longitudinal direction, and (b) in the lateral direction

Figures 5.11(a) and (b) show the distribution of overlay's slippage at the contact surface. The slipping only occurs in the vicinity of the loading area. The friction makes the slippage decrease rapidly and hence negligible at the center to the edges.

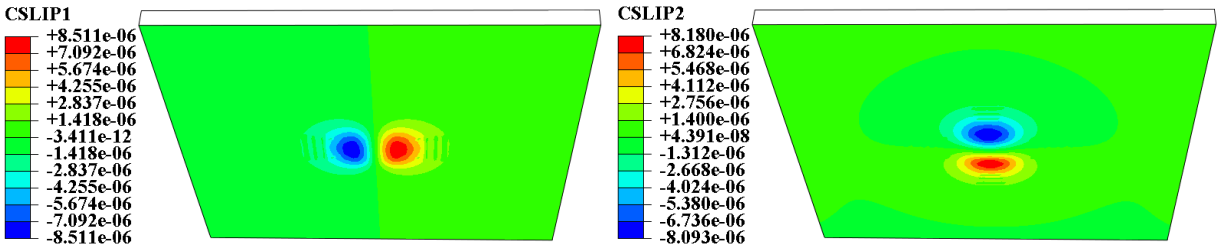

(a) (b)

Figure 5.11 Slipping at contact face (bottom) of overlay: (a) in the longitudinal direction, and (b) in the lateral direction

Figures 5.12(a) to (d) show the normal stress in substrate concrete. Similar to the overlay, the stress in the substrate concrete is localized near the loading area. Compared to the overlay, the maximum normal stress is 0.017 MPa in substrate, which is approximately 10% of 0.17 MPa, the maximum normal stress in overlay. This is due to the separation between the overlay and substrate since it isolates the strain transfer at the interface to some degree. At the interface, only a very small portion of the deformation can be transferred from overlay to substrate concrete via friction. However, much more compression can be transferred. The magnitude of maximum compressive stress in substrate concrete reaches 0.31 MPa, which is about 57% of 0.54 MPa or the magnitude of maximum compressive stress in overlay. The decrease from 0.54 to 0.31 MPa is due to load distribution effect via the overlay.

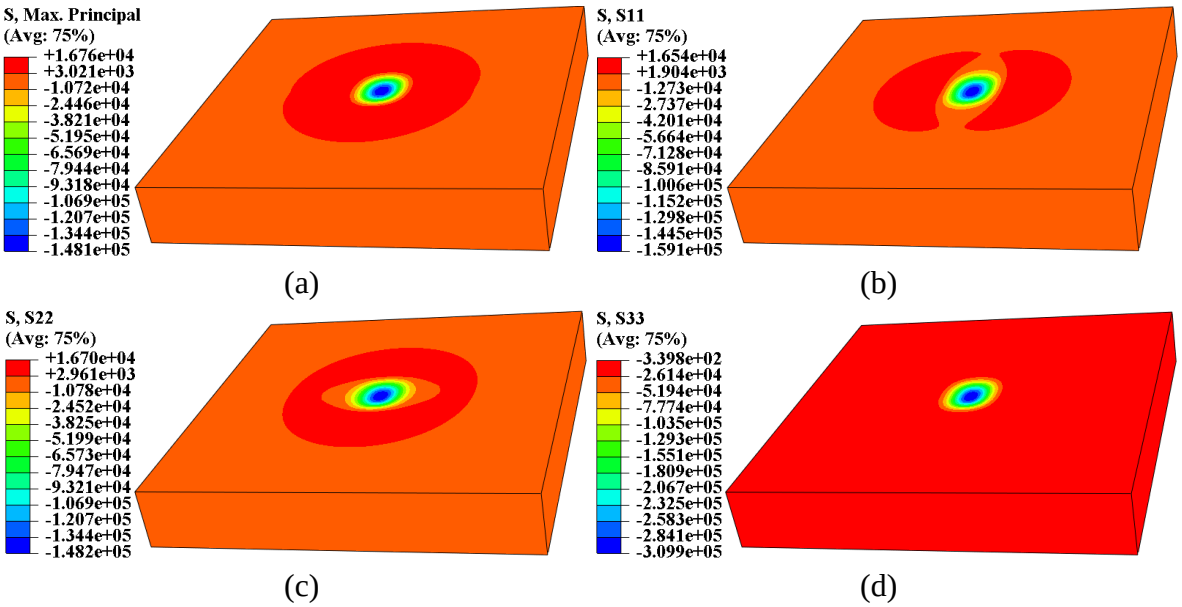

Figure 5.12 Normal stress at contact face (top) of the substrate: (a) maximum principal, (b) longitudinal, (c) transverse, and (d) vertical

Figures 5.13(a) to (d) show the normal strain in the substrate concrete, which are in agreement with the results shown in figures 5.12 (a) to (d).

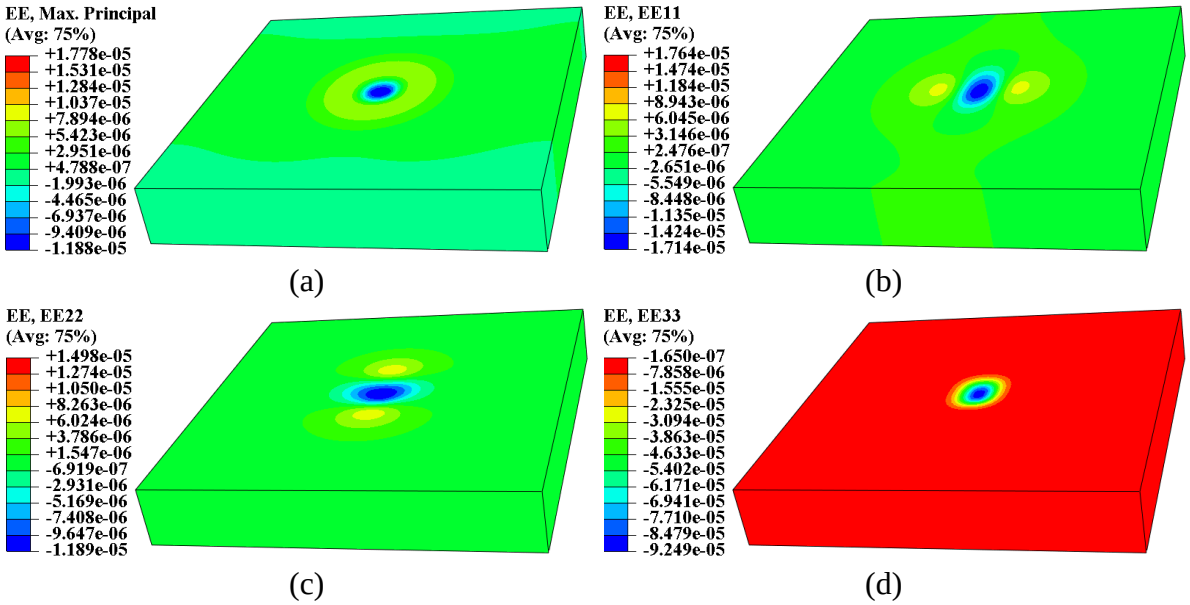

Figure 5.13 Normal strain at contact face (top) of the substrate concrete: (a) maximum principal, (b) longitudinal, (c) transverse, and (d) vertical

5.3.2 Single-Wheel Load at Edge

Figures 5.14(a) to (d) show the normal stress in the overlay. The center of the overlay is in tension at the bottom with a tensile stress of 0.41 MPa or 77% of the applied pressure 0.53 MPa.

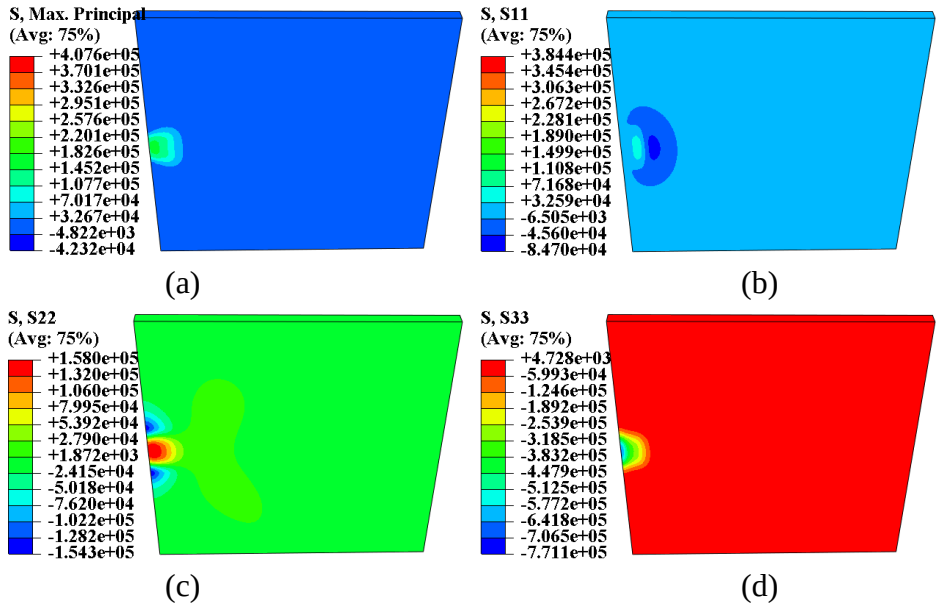

Figure 5.14 Normal stress at contact face (bottom) of the overlay: (a) maximum principal, (b) longitudinal, (c) transverse, and (d) vertical

Compared with the overlay loaded by a single-wheel load at center, the maximum principal stress is increased from 0.17 to 0.41 MPa. The significant increase is mainly due to the decrease of contact area under the loading area. When the wheel load is transferred from top to bottom of the overlay panel, the load is distributed with a spread angle, and thus the contact area is increased. Since the wheel load is distributed over the contact area, the increase of area reduces the maximum contact pressure. However, when the tire is acted along the edge, there is insufficient area for full distribution of the wheel load. Therefore, the maximum contact pressure is increased.

Figures 5.15(a) to (d) show the normal strain in the overlay concrete. The center of the overlay is in tension at the bottom with a tensile strain of 174 με.

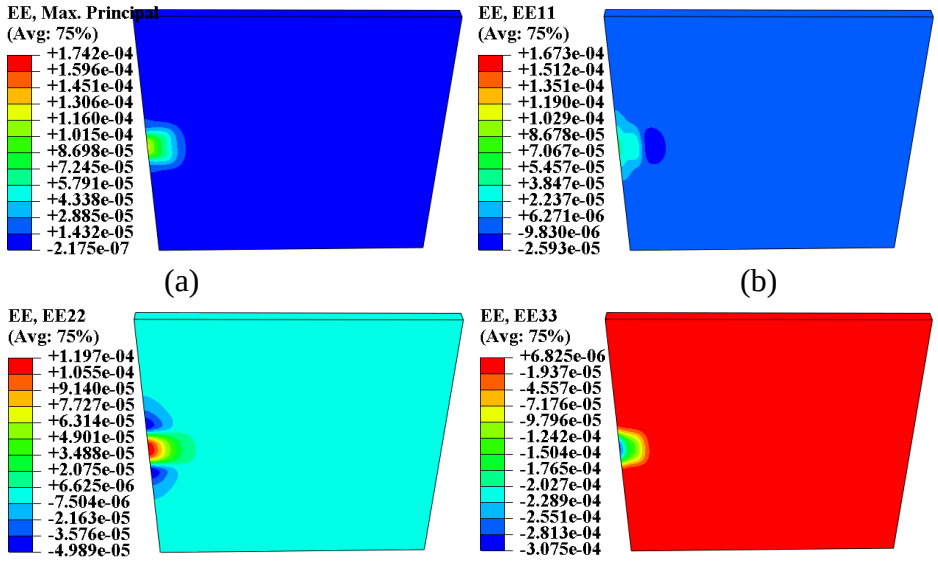

Figure 5.15 Normal strain at contact face (bottom) of the overlay: (a) maximum principal, (b) longitudinal, (c) transverse, and (d) vertical

Figures 5.16(a) and (b) show the contact status and the contact pressure, respectively. The overlay is not in direct contact with the substrate in the vicinity of the center. Although the self-weight of overlay panel tends to limit the opening width, the wheel load is dominant, resulting in significant opening.

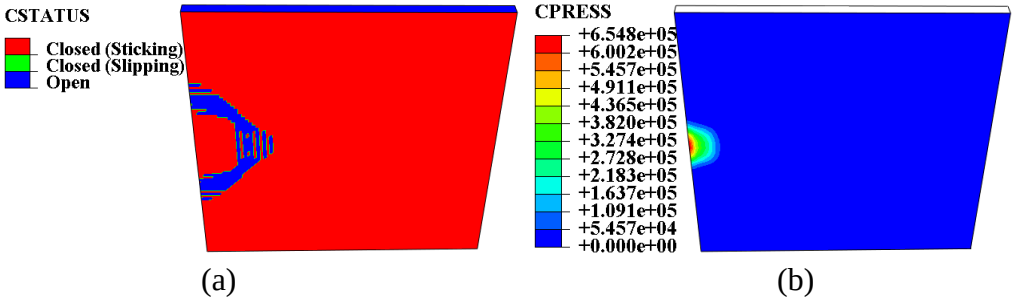

Figure 5.16 Contact behavior in the normal direction: (a) contact status, and (b) contact pressure

Due to opening, the vertical load is resisted by a localized area only, which increases the contact pressure. With a 0.53-MPa tire pressure applied, the maximum contact pressure is 0.65 MPa, as shown in figure 5.16(b). It is about 123% of the applied stress and over twice the contact pressure (0.32 MPa) when the load is applied at the center, shown in figure 5.9(b).

The vertical displacement and the opening width at interface of the overlay and its substrate are shown in figures 5.17(a) and (b), respectively. It is confirmed that the overlay is separated from the substrate under combined wheel load and concrete weight. Figures 5.18(a) and (b) show the shear stress distribution at the contact surface resulting from the friction effect. Figures 5.19(a) and (b) show the distribution of overlay's slippage at the contact surface.

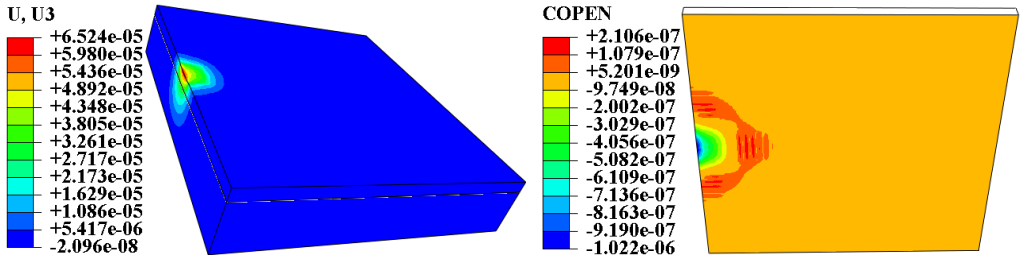

(a) (b)

Figure 5.17 Response of the substrate: (a) vertical displacement (×1000), and (b) opening width

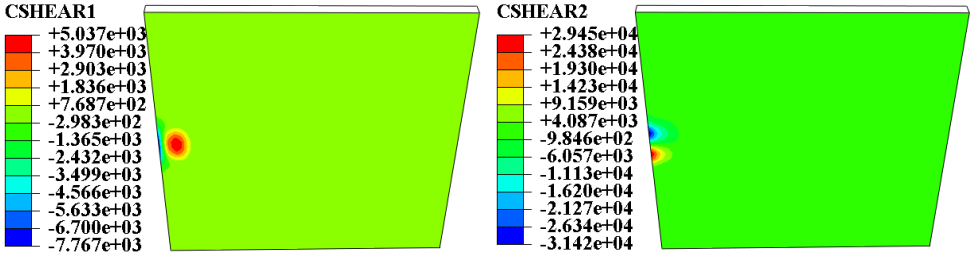

(a) (b)

Figure 5.18 Shear stress distribution at contact face (bottom) of the overlay: (a) longitudinal, and (b) transverse

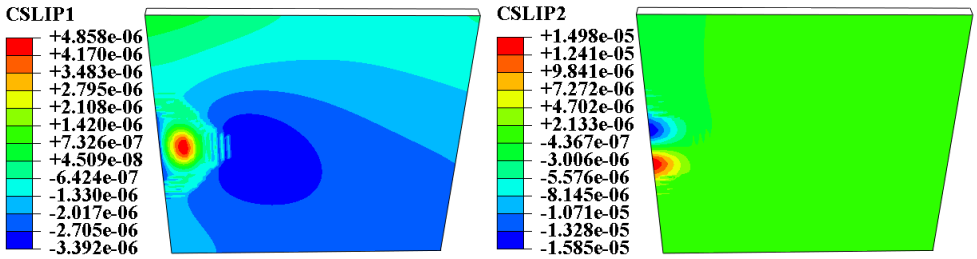

(a) (b)

Figure 5.19 Slipping at contact face (bottom) of the overlay: (a) longitudinal, and (b) transverse

Figures 5.20(a) to (d) show the normal stress in the substrate concrete when loaded to a single-wheel load at edge. The maximum principal stress is approximately 0.031 MPa or 8% of the maximum principal stress in the overlay (0.38 MPa). The maximum compressive stress is 0.61 MPa, which is approximately 79% of 0.77 MPa, the maximum compressive stress in the overlay.

The substrate is subjected to higher stress when loaded at edge due to the reduction of contact area than that when loaded at center. Specifically, the maximum principal stress is increased from 0.017 when loaded at center to 0.031 MPa when loaded at edge. Correspondingly, and the maximum compressive stress is increased from 0.31 to 0.61 MPa. Figures 5.21(a) to (d) show the normal strain in the substrate concrete, which are consistent with the stresses shown in figure 5.20.

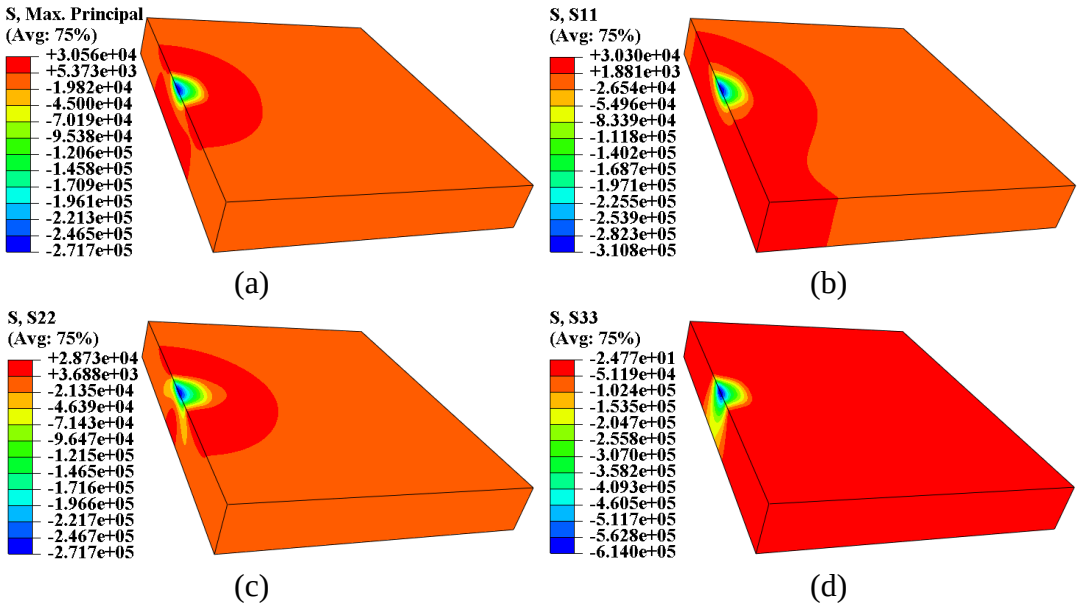

Figure 5.20 Normal stress in the substrate: (a) maximum principal, (b) longitudinal, (c) transverse, and (d) vertical

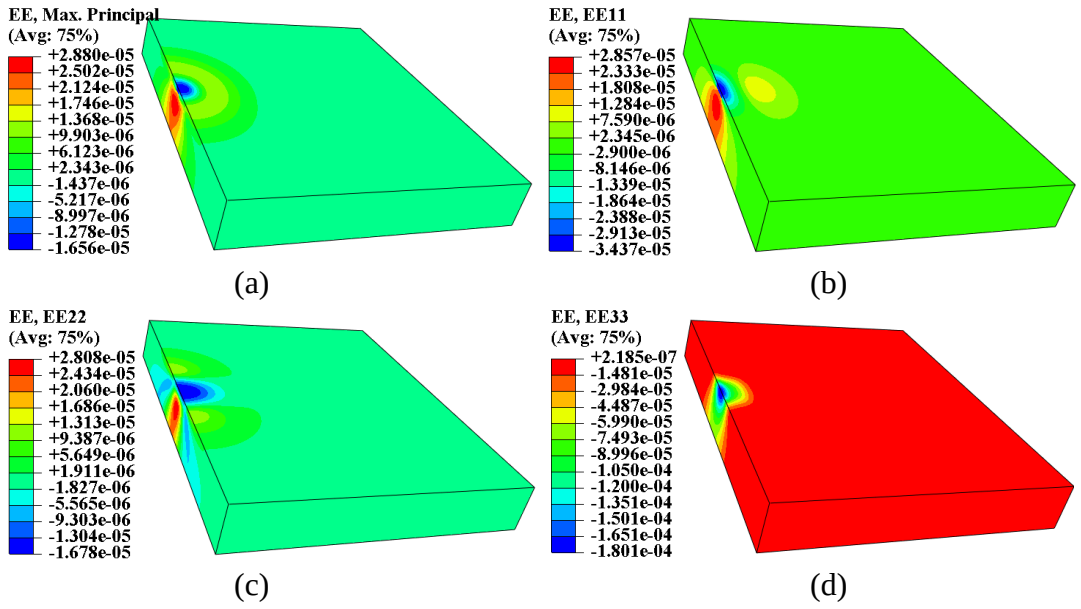

Figure 5.21 Normal strain in the substrate: (a) maximum principal, (b) longitudinal, (c) transverse, and (d) vertical

5.3.3 Double-Wheel Load at Center

Figures 5.22(a) to (d) show the normal stress in the overlay concrete subjected to single-wheel loads at center. The bottom of the overlay at center is in tension with a tensile stress of about 0.076 MPa, which is 36% of the applied stress 0.21 MPa. Correspondingly, Figures 5.23(a) to (d) show the normal strain in the overlay concrete. The bottom of the overlay at center is in tension with a tensile strain of about 38 με.

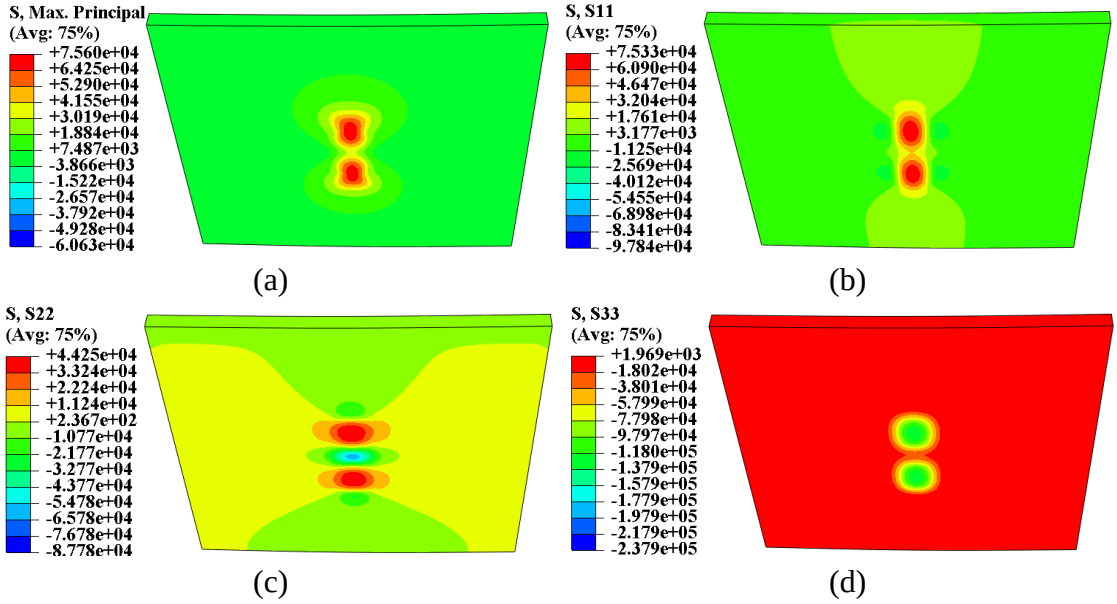

Figure 5.22 Normal stress at contact face (bottom) of the overlay: (a) maximum principal, (b) longitudinal, (c) transverse, and (d) vertical

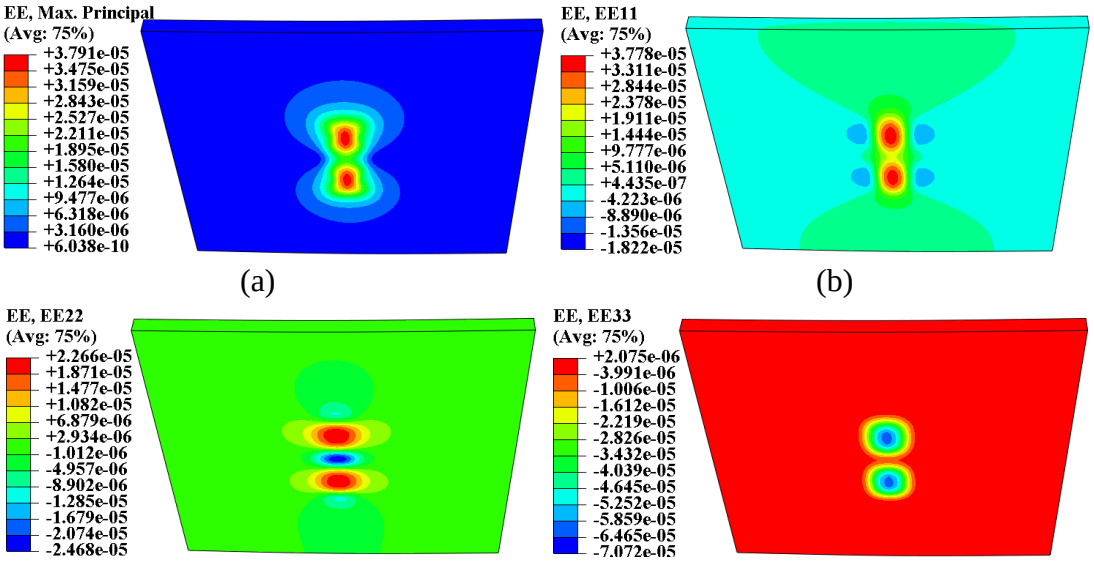

Figure 5.23 Normal strain at contact face (bottom) of the overlay: (a) maximum principal, (b) longitudinal, (c) transverse, and (d) vertical

Figures 5.24(a) and (b) show the contact status and the vertical displacement, respectively. Except for the center area under wheel loads, the overlay is not in direct contact with the substrate. The mechanism of the opening is illustrated in figure 5.7.

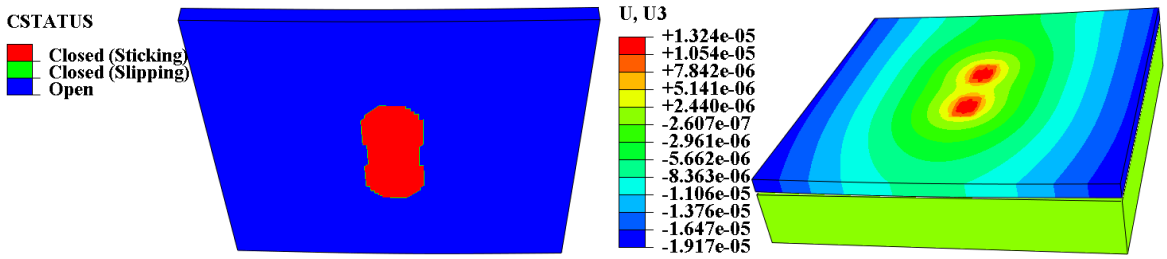

Figure 5.24 Contact behaviour between the overlay and its substrate: (a) contact status, (b) vertical displacement

Figures 5.25(a) and (b) show the opening width and the contact pressure, respectively. The edges go upward relative to the substrate with a maximum separation distance of about 0.02 mm. The maximum contact pressure is 0.13 MPa, which is about 62% of the applied stress. This reduction is due to the load distribution via the overlay concrete.

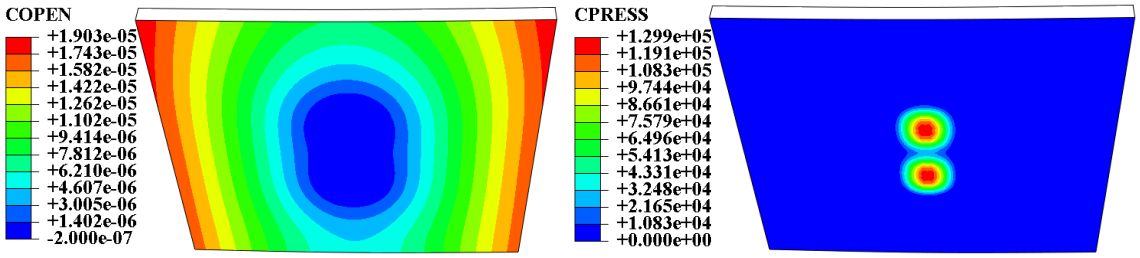

(a) (b)

Figure 5.25 Contact behavior in normal direction: (a) contact opening width, and (b) contact pressure

Figures 5.26(a) and (b) show the shear stress distribution at the contact surface, which results from the friction. Correspondingly, figures 5.27(a) and (b) show the distribution of overlay's slippage at the contact surface.

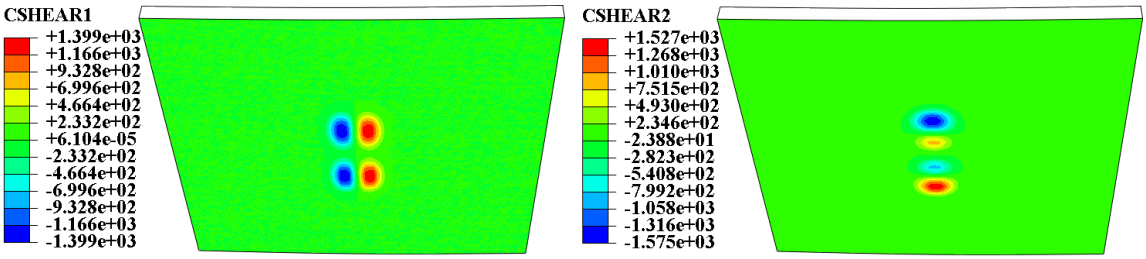

(a) (b)

Figure 5.26 Shear stress distribution at contact (bottom) face of substrate: (a) longitudinal direction, and (b) lateral direction

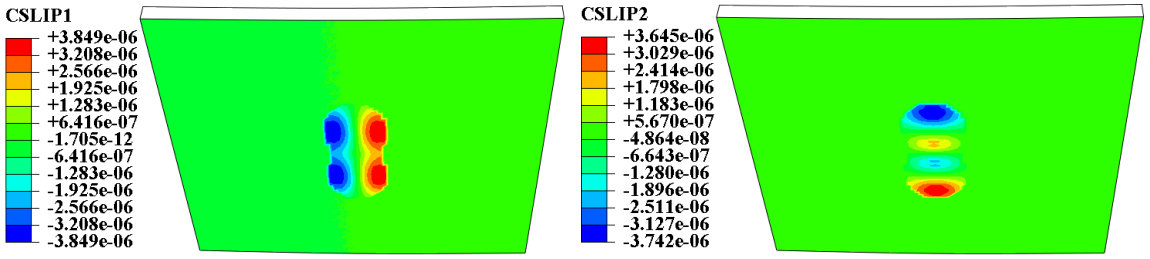

(a) (b)

Figure 5.27 Slipping at contact face (bottom) of the overlay: (a) longitudinal, and (b) transverse

Figures 5.28(a) to (d) show the normal stress in the substrate concrete when the overlay is subjected to a double-wheel load at center. The maximum principal stress is approximately 0.009 MPa, which is about 12% of the maximum principal stress in the overlay (0.076 MPa). The maximum compressive stress is 0.13 MPa, which is about 54% of the maximum compressive stress in the overlay (0.24 MPa). Figures 5.29(a) to (d) show the corresponding normal strain in the substrate concrete.

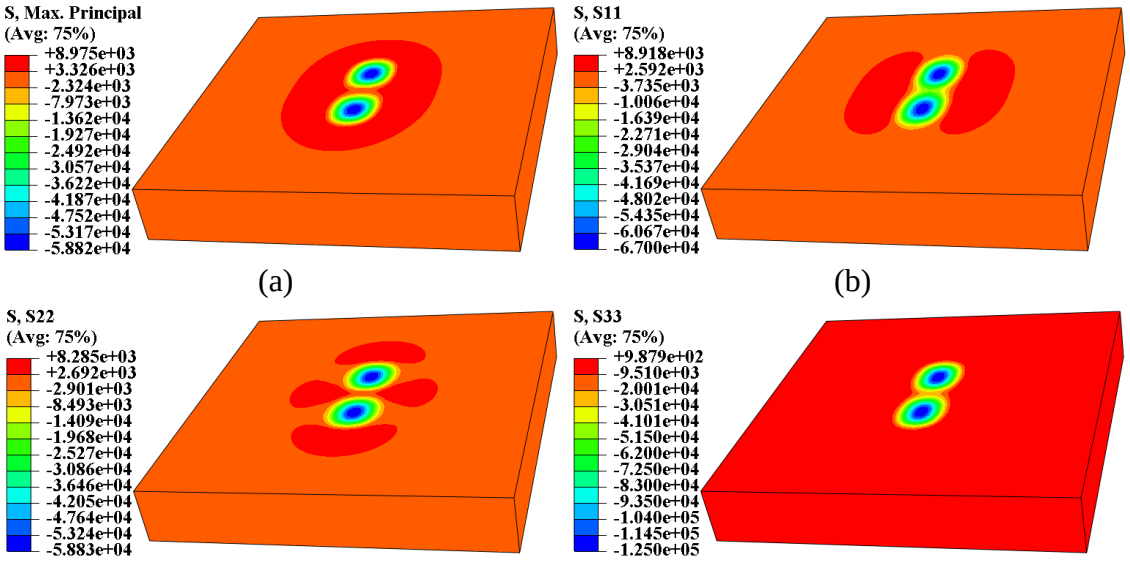

(a) (b)

(c) (d)

Figure 5.28 Normal stress at contact face (top) in the substrate: (a) maximum principal, (b) longitudinal, (c) transverse, and (d) vertical

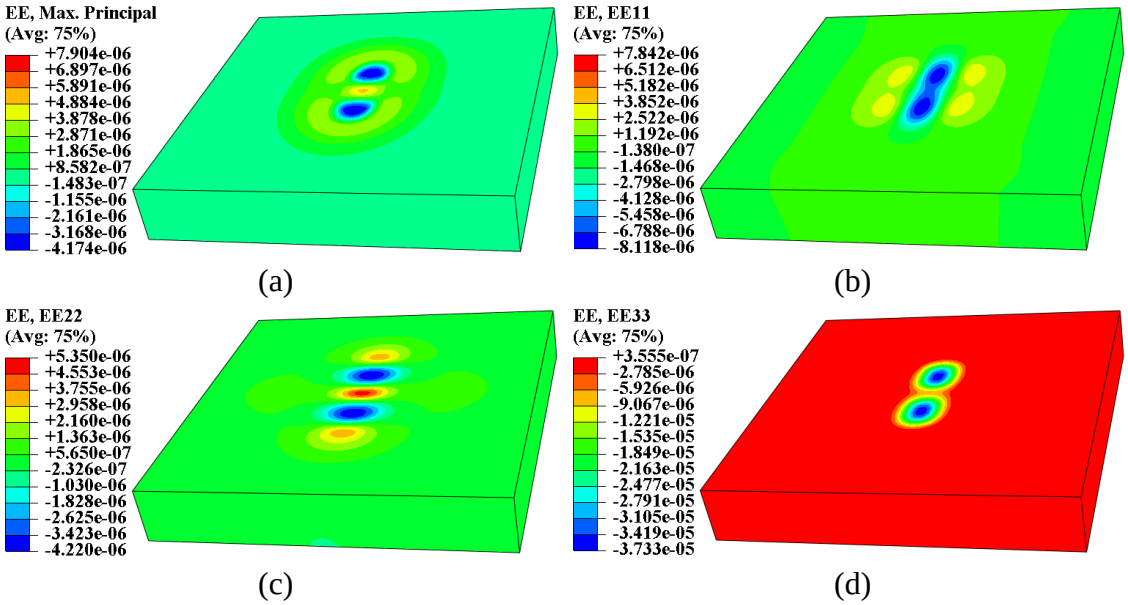

Figure 5.29 Normal strain at contact face (top) of the substrate: (a) maximum principal, (b) longitudinal, (c) transverse, and (d) vertical

5.3.4 Double-Wheel Load at Edge

Figures 5.30(a) to (d) show the normal stress in the overlay concrete when subjected to a single-wheel load at edge. The bottom of the overlay at edge is in tension with a tensile stress of approximately 0.16 MPa, which is about 76% of the applied stress 0.21 MPa.

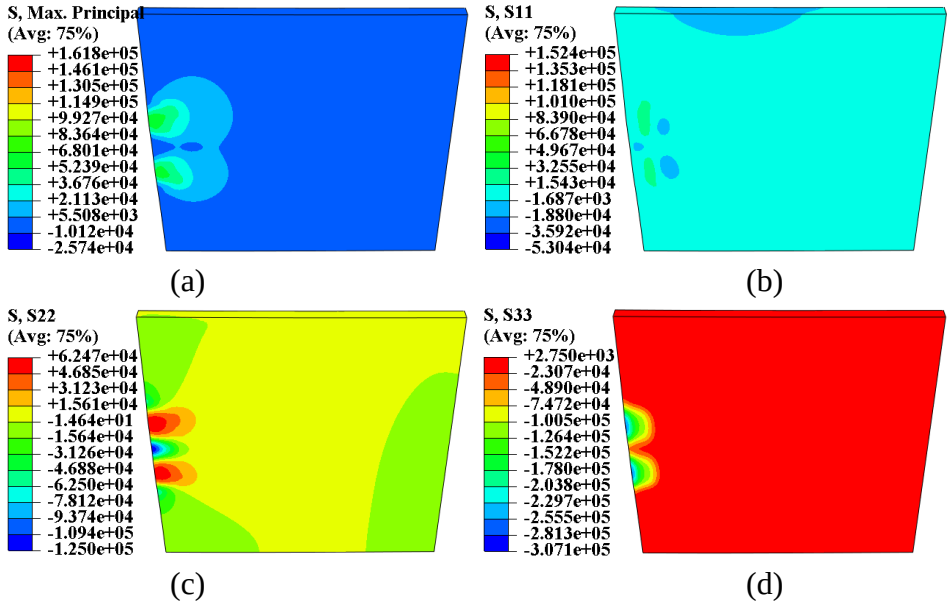

Figure 5.30 Normal stress at contact face (bottom) of the overlay: (a) maximum principal, (b) longitudinal, (c) transverse, and (d) vertical

Figures 5.31(a) to (d) show the normal strain in the overlay when subjected to a single-wheel load at edge. The bottom of the overlay is in tension with a tensile stress of approximately 38 με.

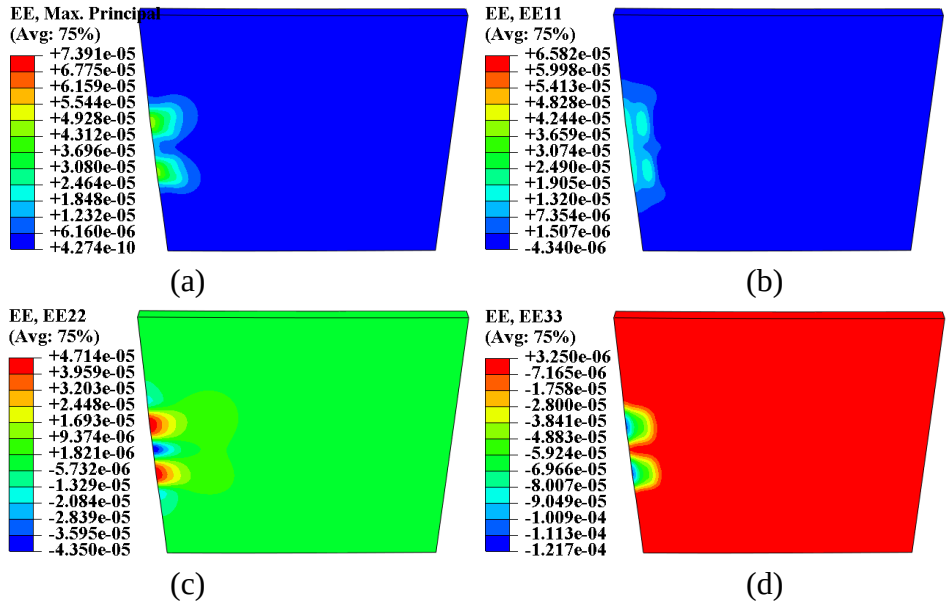

Figure 5.31 Normal strain at contact face (bottom) of the overlay: (a) maximum principal, (b) longitudinal, (c) transverse, and (d) vertical

Figures 5.32(a) and (b) show the contact status and the contact pressure, respectively. Except for the edge area under wheel loads, the overlay is not in direct contact with the substrate. Figures 5.33(a) and (b) show the vertical displacement and the contact opening width, respectively.

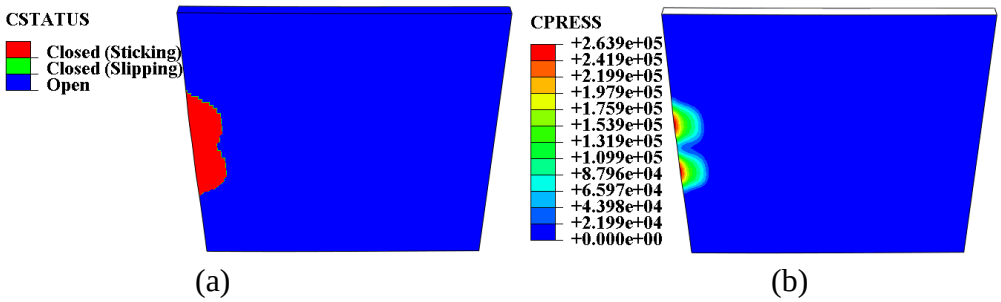

Figure 5.32 Contact behavior of the overlay: (a) contact status, and (b) contact pressure.

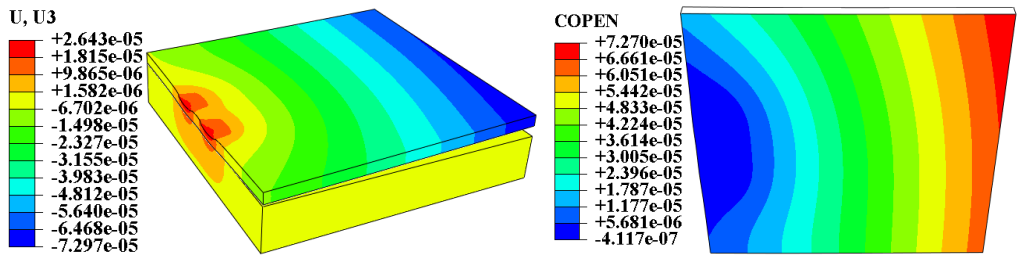

(a) (b)

Figure 5.33 Contact behavior in normal direction: (a) vertical displacement, and (b) opening width

Figures 5.34(a) and (b) show the shear stress distribution at the contact surface resulting from friction. Correspondingly, Figures 5.35(a) and (b) show the distribution of overlay's slippage.

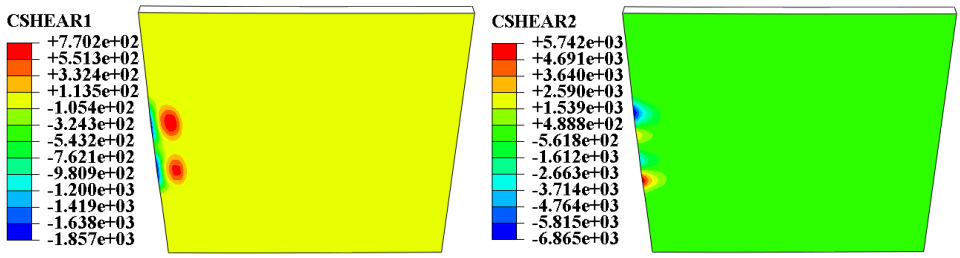

(a) (b)

Figure 5.34 Shear stress distribution at interface: (a) longitudinal, and (b) transverse

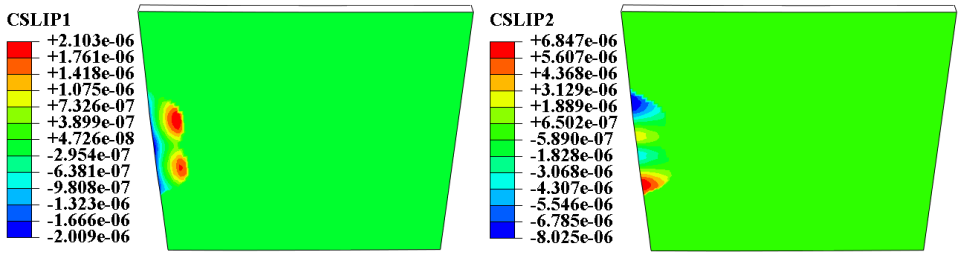

(a) (b)

Figure 5.35 Slipping at interface: (a) longitudinal, and (b) transverse

Figures 5.36(a) to (d) show the normal stress in the substrate concrete when the overlay is subjected to a double-wheel load at edge. The maximum principal stress is approximately 0.017 MPa, which is about 10% of the maximum principal stress in the overlay (0.17 MPa). The maximum compressive stress is 0.25 MPa, which is about 81% of the maximum compressive stress in the overlay (0.31 MPa).

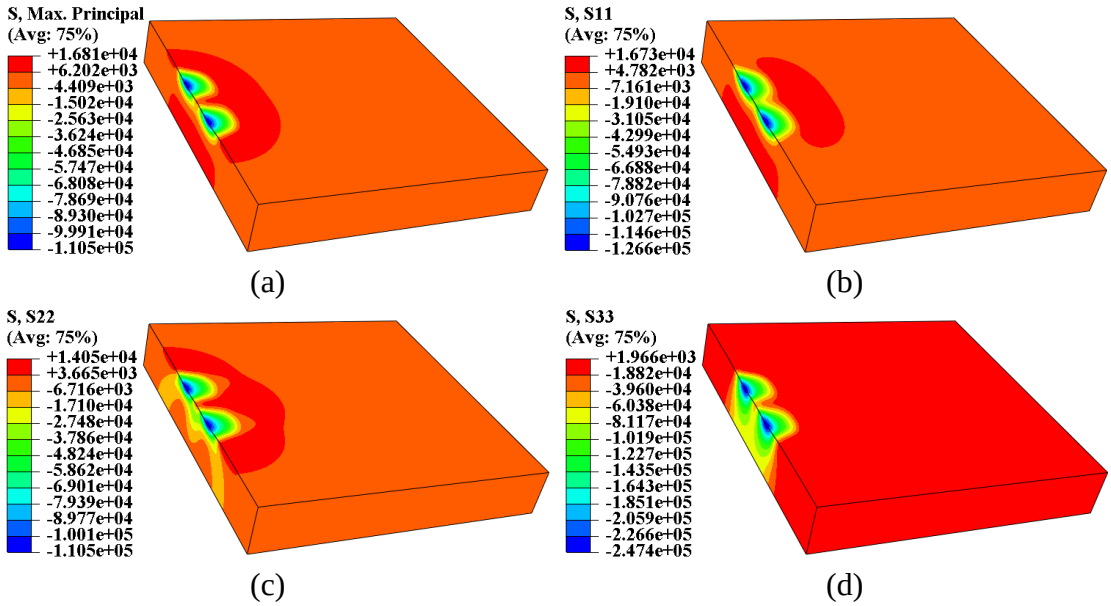

Figure 5.36 Normal stress of the substrate: (a) maximum principal, (b) longitudinal, (c) transverse, and (d) vertical

Figures 5.37(a) to (d) show the normal strain in the substrate concrete when the overlay is subjected to a double-wheel load at edge.

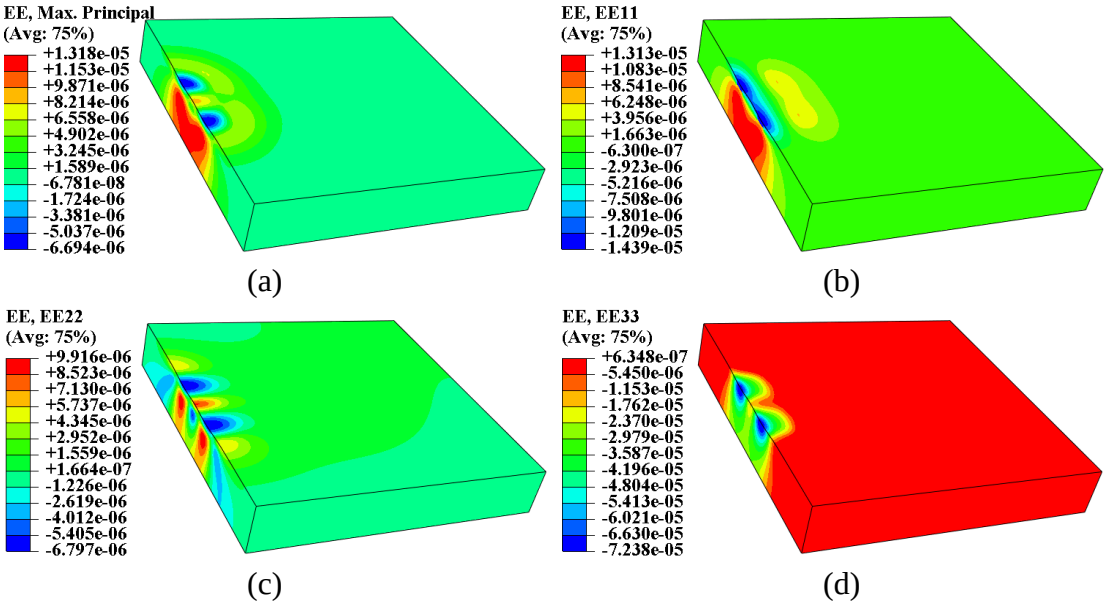

Figure 5.37 Normal strain of the substrate: (a) maximum principal, (b) longitudinal, (c) transverse, and (d) vertical

5.4 Summary

Numerical simulations are carried out to determine the stress and strain distributions in an unbonded pavement system under different loading cases. The primary findings are summarized below:

(1) The bottom of the overlay under the wheel loads is subjected to tension. The maximum principal stress is approximately 32~36% of the pressure applied on the tire at center of the overlay, and 76~77% of the pressure applied on the tire at edge.

(2) The maximum principal stress in the substrate is tensile, and its magnitude is approximately 8~12% of the maximum principal stress in the overlay. Under loads at center, the maximum compressive stress in the substrate is approximately 54~57% of that in the overlay. Under loads at edge, the maximum compressive stress in the substrate is approximately 76~79% of that in the overlay.

(3) The distribution of contact pressure between the overlay and its substrate concrete is not uniform. The area under wheel loads is subjected to high pressure while the other area is either zero or close to zero. Except for the area under wheel loads, the other area is not in direct contact with the substrate.

Chapter 6 Laboratory Study on Dislocation of Bonded Concrete Overlay

6.1 Introduction

Concrete pavement overlays can be used as a time-saving and cost-effective alternative for replacement of existing pavement. For a pavement in good condition, a thin concrete layer can be cast on top to increase the pavement thickness. However, for a pavement with cracks and significant deterioration, the thin overlay is vulnerable to reflection cracks. In that scenario, unbonded pavement overlay can be considered for minimum impact by existing cracks in substrate, which is the subject investigated in chapters 3 through 5.

Besides the reflection crack in substrate, temperature gradients and differential volume changes can cause cracking in overlay. For bonded overlays, the substrate restrains the deformation of overlay associated with shrinkage-induced volume change since the volume of the existing substrate is relatively stabilized. Thus, there are tensile strains induced in the overlay and at the interface between old and new concrete, resulting in cracks and delamination (Lange and Shin 2001, Shin and Lange 2004, Shin and Lange 2012).

In the past two decades, ultra-high performance concrete (UHPC) has gained increasing interest in the research community due to its high mechanical strengths, low permeability that leads to good durability, and excellent workability. The superior mechanical properties make it promising for fabricating ultra-thin overlays for reconstruction or rehabilitation of highway roadway. However, the shrinkage-induced strain could be problematic due to its potential cracking issues caused by autogenous or drying shrinkage. Although fibers can be used to increase the tensile strength and thus improve the cracking resistance, delamination at interface can result in curling and thus eventually lead to failure of the overlay due to external wheel loads or temperature effects (Lange and Shin 2001, Shin and Lange 2004, Shin and Lange 2012).

Identification of cracks and delamination at early age enables timely and cost-effective renovation and thus significantly extends the service life of the pavement. In the literature, a variety of delamination detection technologies based on optical fiber have been proposed due to their advantages, such as immunity to electromagnetic interference (EMI), compactness, light weight, resistance to harsh environment, multiplexing ability, and distributed sensing ability. According to the spatially sensing range, fiber optic sensors can be categorized into point or localized sensors and distributed sensors. A point sensor gives a reading that represents the overall effect over its gage length. However, a distributed sensor allows continuous measurement over its entire length. Some point sensors, such as fiber Bragg grating (FBG) and interferometer sensors, can be multiplexed in series to form a quasi-distributed sensor, which gives readings at some discrete points. Both point and distributed sensors have been implemented to detect cracks and delamination in various composites.

FBG sensors have been used to detect cracks or delamination in laminated composites. For an embedded FBG sensor, a crack or delamination crossing its gratings can result in a non-uniform or differential strain field that causes broadening of the reflection spectrum of the Bragg gratings in the optical fiber. Based on theoretical or numerical studies, the change of spectrum can be correlated with the crack width or delamination in the composites (Propst et al. 2010, Ling et al. 2005, Childs et al. 2008).

A Michelson interferometer sensor was mounted on the surface of unidirectional carbon fiber-reinforced epoxy composites to detect damage. The response of the interference signal to either dynamic or static loading was investigated. Through a digital filtering technique, real-time information comparable to acoustic emission (AE) data could be obtained from the interferometer output to reflect the presence of damage. However, the location and extent of the

damage cannot be obtained (Tsuda et al. 1999).

An embedded Mach-Zehnder interferometer sensor was used to detect delamination in a composite beam under quasi-impulse loading. Delamination can be identified as a sudden 'jump' in magnitude of the normalized integral strain versus load position curve, and the delamination size and location were evaluated (Leung et al. 2005, Jiang et al. 2009).

However, a large number of sensors are required to monitor cracks or delamination in a relative large area since the location of cracks and delamination cannot be predicted accurately. In addition, the requirement for many sensors could be cost prohibitive in practical applications. In this sense, a distributed fiber optic sensor may be a good alternative.

Optical fiber was embedded in composite tubes to detect impact damage with Rayleigh scattering-based optical time domain reflectometry (OTDR) technology. The optical fiber was directly incorporated into filament-wound tubes during manufacturing, and ruptured when they experienced a direct impact. The rupture of the optical fiber can result in significant attenuation of the transmitted light. By measuring the change of transmitted light intensity due to the impact event, the damage state can be indicated. However, since this method relies on the break of optical fiber, once damage is detected by an optical fiber, the fiber will not be able to sense the damage occurring at a further distance (Martin et al. 1997).

Brillouin optical time domain reflectometry (BOTDR) and Brillouin optical time domain analysis (BOTDA) technologies have been developed based on Brillouin scattering in optical fiber, which allows simultaneous measurement of strain and temperature changes. Since BOTDR is based on spontaneous Brillouin scattering, both incident and backscattered signals are at the same end, and thus it only needs one-end measurement. However, BOTDA is based on stimulated Brillouin scattering. The pump and probe waves are input from two ends,

respectively, and thus BOTDA requires two-end measurement. The spatial resolution of the conventional BOTDR and BOTDA technologies are limited to the order of half a meter, which makes it challenging to provide satisfactory results for delamination detection. Recently, pre-pump pulse BOTDA or PPP-BOTDA technology was developed, allowing measurements with 2-cm spatial resolution. Embedded capillary sensors and comparative vacuum monitoring (CVM) techniques were successfully applied to detect delamination in carbon fiber reinforced plastic structures (Minakuchi et al. 2012). However, the proposed method largely relied on the employment of embedded capillary sensors, which makes it inconvenient and costly in practical applications in the pavement field.

In this study, a delamination detection method is proposed for bonded concrete pavement overlay systems using telecom grade single mode optical fibers with PPP-BOTDA. A simple deployment applicable for practical pavement construction is presented, allowing continuous detection of delamination along the fiber length.

6.2 Specimen and Instrumentation

Concrete pavement specimens instrumented with distributed fiber optic sensors were designed and fabricated, as shown in figure 6.1. Each specimen was composed of a 200-mm-thick substrate layer made of conventional concrete, and a 50-mm-thick pavement overlay made of UHPC. Table 6.1 gives the composition of the UHPC mixture.

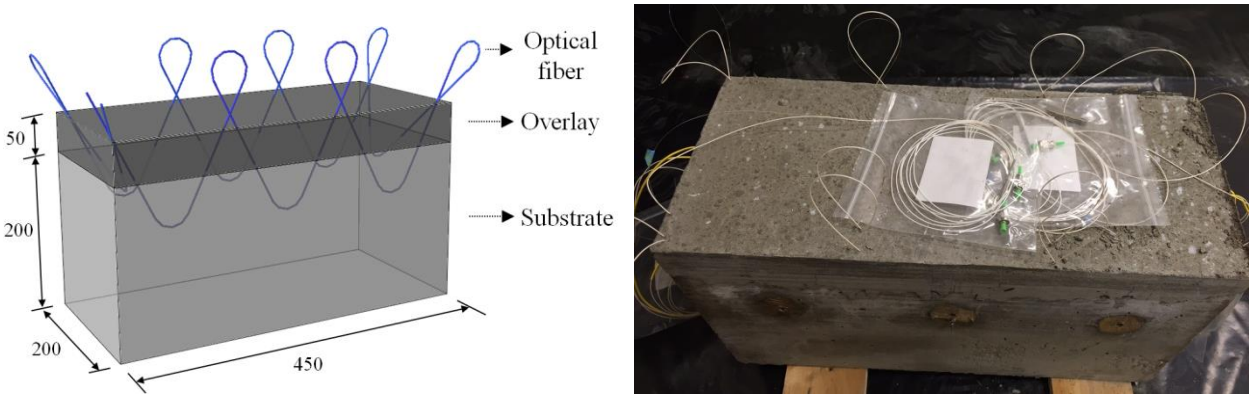

(a) (b)

Figure 6.1 Concrete pavement specimen: (a) schematic view (unit: mm), (b) real specimen

Each specimen was instrumented with two types of single mode optical fiber: bare fiber (BF), as shown in fig 2.4, and fiber with tight buffer (TB), as illustrated in figure 6.2. The tight buffer is bonded with the outer coating, and thus, deformation can be transferred at the interface of shear strain. The tight buffer can significantly enhance the mechanical performance of optical fiber, in particular, shear capacity, ensuring fiber's survival during brutal operations.

Table 6.1 Composition of the UHPC mixture

Materials	**Amount**
Cement (kg/m^3)	593
GGBS (kg/m^3)	546
River sand (0-5 mm) (kg/m^3)	704
Masonry sand (0-2 mm) (kg/m^3)	298
HRWR (l/m^3)	54.2
Water (kg/m^3)	173.7
Steel fibers (kg/m^3)	156

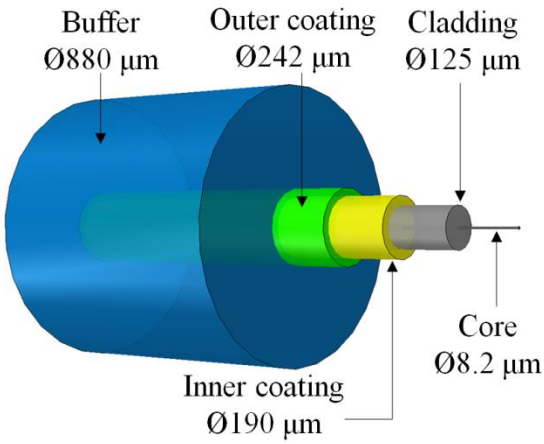

Figure 6.2 Single mode optical fiber packaged with tight buffer

The BF and TB sensors were deployed closely in parallel in each specimen, as shown in figure 6.1(a). The sensors were first installed in a wood formwork in a predetermined pattern, then cast in part into the concrete substrate, and finally cast into the UHPC overlay after the substrate was wet cured for 28 days at room temperature. Each distributed sensor passed the interface between the UHPC and its substrate 16 times, as illustrated in figure 6.3. To compensate for the temperature effect due to concrete hydration, another BF was loosely passed through a polymer hose (1-mm inner diameter and 2-mm outer diameter), which was installed close to and parallel with the other two sensors. Since this BF was not bonded to the polymer hose, it did not sense the strain change in concrete.

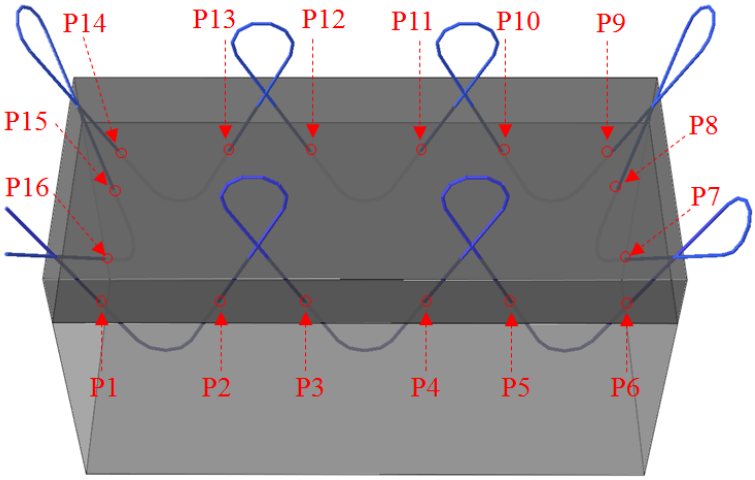

Figure 6.3 Intersections of optical fiber with UHPC-substrate concrete interface

6.3 Experiments

A Brillouin frequency distribution was measured from each distributed fiber optic sensor using Neubrescope with PPP-BOTDA, as shown in Figure 6.4. The two ends of each sensor were connected to the Neubrescope through transmission cables. The measured Brillouin frequency distribution can be converted into its corresponding strain distribution. Measurements were taken at various curing ages or 1, 2, 3, 7, 14, 21, and 28 days after the concrete setting.

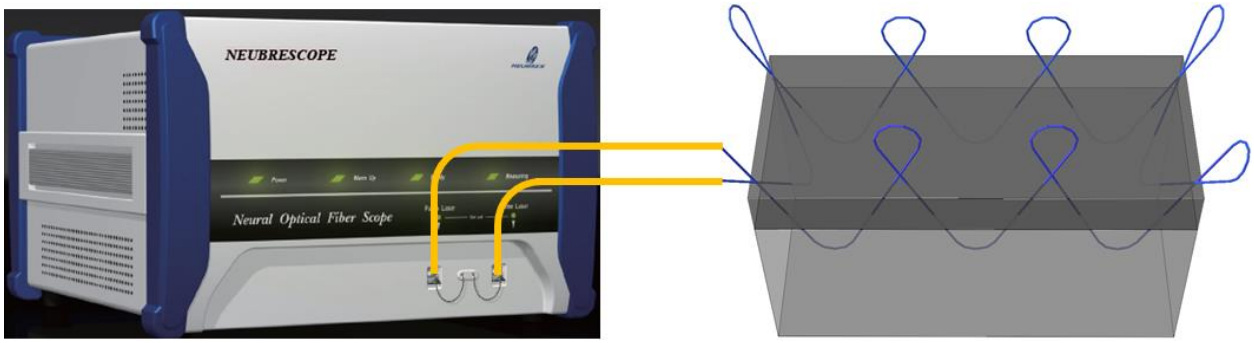

Figure 6.4 Test setup

Both autogenous and drying shrinkage-induced strains in the UHPC overlay were measured in accordance with ASTM standards at different curing ages. The age for measurement of the autogenous shrinkage was counted from concrete setting, and the age for drying shrinkage was counted after 3-day wet curing of the concrete.

6.4 Test Results and Discussion

The Neubrescope measures the Brillouin frequency distribution along the length of each distributed sensor, which can be converted into corresponding strain distribution. Figures 6.5(a) and (b) show converted strain distributions from the two distributed sensors, respectively. The horizontal and vertical axes represent the distance along the distributed sensors, and the measured strain by the sensors. Each figure has four curves corresponding to 1, 3, 7, and 28 days after concrete setting.

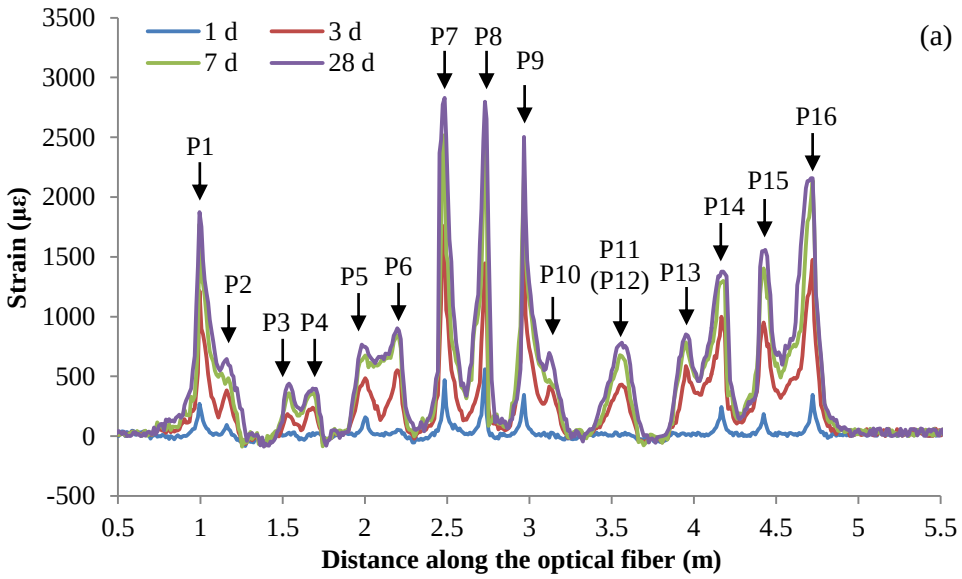

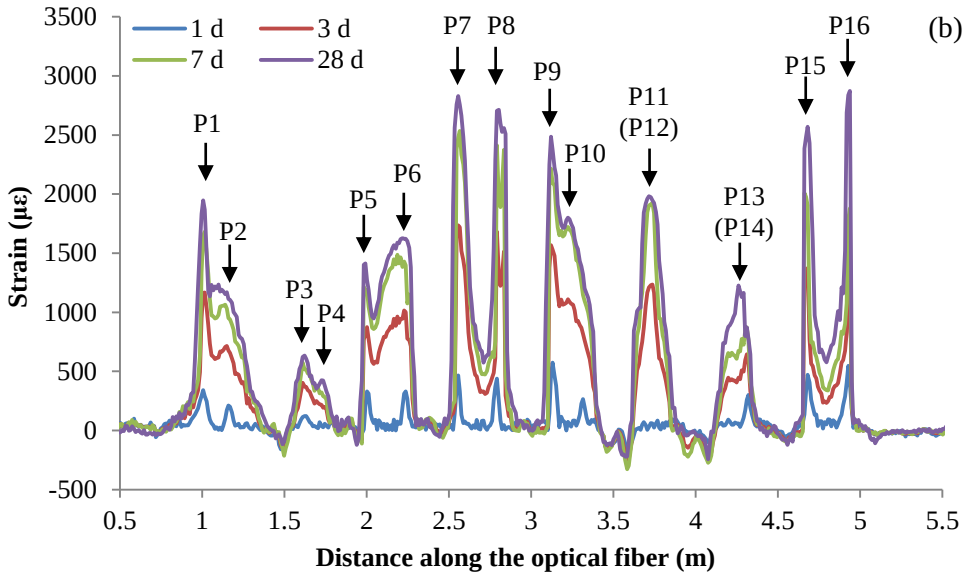

Figure 6.5 Strain distributions: (a) BF sensor, and (b) TB sensor

It can be observed from figure 6.5 that each curve has multiple sharp peaks that correspond to delamination points at the interface of UHPC overlay and its substrate. When delamination occurred, the overlay slightly curled and was separated from its substrate. Since each fiber optic sensor was embedded and bonded with surrounding concrete, the appearance of a separation or delamination between the UHPC overlay and its substrate locally stretched the fiber with a sudden change of strain at the delamination face, which can thus be identified as a sharp peak in the strain distribution.

Locations of the peaks can be correlated to the intersections of the fiber with the UHPC-substrate interface, as shown in figure 6.3. Hence, delamination can be located from the measured strain distribution. Both visible and hidden cracks at the delamination interface can be detected as long as they passed through the optical fiber. When the distance between two adjacent peaks is small, the peaks may merge into one peak due to finite spatial resolution. For example, in figure 6.5(a), the peaks corresponding to P11 and P12, respectively, cannot be

distinguished.

The onset and propagation of delamination can be detected from a strain distribution. For instance, in figure 6.5(a), the delamination at P5 appeared in the first day measurement, while no delamination occurred at P6 at the same time. The delamination could be detected in the third day measurement, indicating that the delamination at P6 happened between the first and third days. Furthermore, the increase in magnitude of each peak indicates the widening of a delamination induced open.

Figure 6.6 shows a concrete specimen after 28-day air curing. A crack can be visibly observed at the interface between the UHPC overlay and its substrate, proving statements on delamination based on the measurement results from distributed sensors.

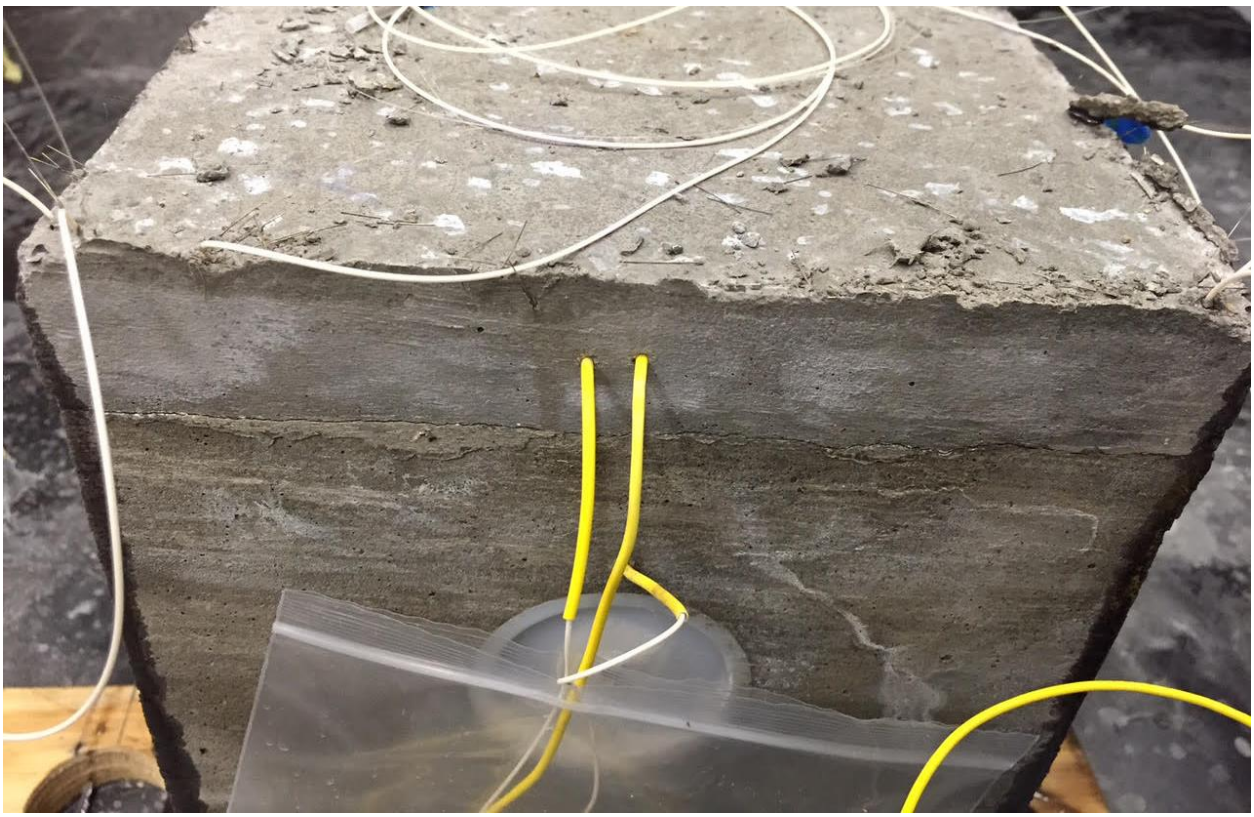

Figure 6.6 UHPC overlay specimen after 28-day air curing

The delamination resulted from the difference of strain changes in the substrate and UHPC overlay. After the substrate concrete was air cured for 28 days, most shrinkage finished and the substrate can then be considered as free of shrinkage-induced strain change after the UHPC overlay was cast. However, the UHPC was subjected to shrinkage, which induced strain difference. Figures 6.7(a) and (b) show the autogenous and drying shrinkages in the UHPC, respectively. At the 28th day, the autogenous and drying shrinkage-induced strains are 253 and 543 με, respectively.

The strain difference in the UHPC and substrate would induce tensile stress at their interface, which could result in delamination.

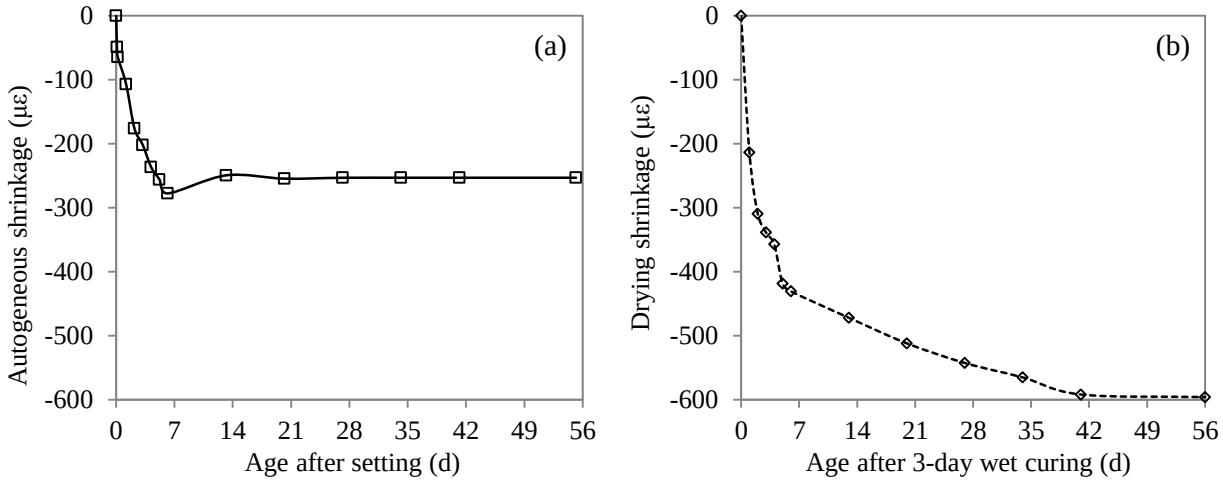

Figure 6.7 Shrinkage induced strains: (a) autogenous shrinkage, and (b) drying shrinkage

6.5 Summary

The delamination phenomenon in UHPC pavement overlay system was investigated and detected using a cost-effectively distributed fiber optic sensor. Primary findings are summarized below:

(1) Shrinkage-induced strain can lead to delamination in the UHPC pavement overlay.

The delamination can occur in the first days after concrete setting.

(2) Distributed fiber optic sensors can be used to detect the delamination of UHPC pavement overlay system. The delamination can be identified as sharp peaks in the measured strain distribution by the distributed sensor with PPP-BOTDA. The onset and propagation of the delamination can be monitored.

Chapter 7 Conclusions

In this report, both experimental and numerical studies on the strain distribution in both unbonded and bonded concrete pavement overlays were carried out. Cracks in the concrete overlay were investigated using distributed fiber optic sensors with PPP-BOTDA measurements.

The strain sensitivity coefficient of the distributed fiber optic sensor was experimentally calibrated to be 0.0541 MHz/με. The mechanical performance of the optical fiber was evaluated. The tensile force capacity is approximately 26 N; the ultimate strain limit is approximately 26,000 με (2.6%).

The distributed sensor was successfully applied to measure autogenous shrinkage in cementitious mortar. The measurement was in agreement with the ASTM standard method. Non-uniform shrinkage was detected by the distributed sensor, and cracks were identified from the peaks of a strain distribution.

To protect fragile optical fibers, cementitious mortar grids instrumented with optical fibers, namely smart grids, were designed and fabricated. The smart grids were successfully implemented in the MnROAD. The overlay was repeatedly loaded using a truck. Crack in the overlay was successfully detected by the distributed sensors.

Numerical simulations were carried out to analyze the stress and strain distributions in the unbonded pavement system under different loading scenarios. The bottom of the overlay is subjected to tension in the area under wheel loads. The maximum principal stress is approximately 32~36% of the pressure applied on the loading tire at center of the overlay. When loaded at edge, the maximum principal stress is approximately 76~77% of the pressure applied on the tire. The maximum principal stress in the substrate is in tension and approximately 8~12% of the maximum principal stress in the overlay. When loaded at center, the maximum

compressive stress in the substrate is approximately 54~57% of that in the overlay. When loaded at the edge, the maximum compressive stress in the substrate is approximately 76~79% of that in the overlay. The distribution of contact pressure between the concrete overlay and its substrate is non-uniform. The pressure in the area of wheel loads is equal to the model value applied on the tire, and the pressure elsewhere is close to zero. When the overlay is subjected to double-wheel loads, opening would occur between the overlay and its substrate concrete. In that case, except for the area under wheel loads, all areas are out of contact with the substrate.

Delamination phenomenon in the UHPC overlay system was investigated and detected using distributed fiber optic sensors. Shrinkage induced strain could lead to delamination in UHPC pavement overlay. The delamination could occur in the first hour after concrete setting. Distributed fiber optic sensors can be used to detect the delamination in the UHPC pavement overlay. The delamination can be identified as sharp peaks in the measured strain distribution, and the onset and propagation of delamination can be monitored.

References

Alahbabi, MN, YT Cho, and TP Newson. “Simultaneous temperature and strain measurement with combined spontaneous Raman and Brillouin scattering.” Opt. Lett. 2005, 30, 1276-1278.

Bao, X, DJ Webb, and DA Jackson. “22-km distributed temperature sensor using Brillouin gain in an optical fiber.” Opt. Lett. 1993, 18, 552–554.

Bao, X, DJ Webb, and DA Jackson. “32km distributed temperature sensor based on Brillouin loss in an optical fiber.” Opt. Lett. 1993, 18, 1561-1563.

Bao, X, J Dhliwayo, N Heron, DJ Webb, and DA Jackson. “Experimental and theoretical studies on a distributed temperature sensor based on Brillouin scattering.” J. Lightwave Technol. 1995, 13, 1340–1348.

Bao, X and L Chen. “Recent progress in Brillouin scattering based fiber sensors.” Sensors 2011, 11, 4152-4187.

Bao, X and L Chen. “Recent progress in distributed fiber optic sensors.” Sensors 2012, 12, pp. 8601-8639.

Bao, Y, W Meng, Y Chen, G Chen, and K Khayat. “Measuring mortar shrinkage and cracking by pulse pre-pump Brillouin optical time domain analysis with a single optical fiber.” Mater. Lett. 2015, 145, 344-346.

Barnoski, MK, MD Rourke, SM Jensen, and RT Melville. “Optical time domain reflectometer.” Appl. Opt. 16 (1977), pp. 2375-2379.

Belal, M, YT Cho, M Ibsen, and TP Newson. “A temperature-compensated high spatial resolution distributed strain sensor.” Meas. Sci. Technol. 2010, 21, 015204.

Bernini, R, A Minardo, and L Zeni. “Accurate high-resolution fiber-optic distributed strain measurements for structural health monitoring.” Sensors and Actuators A 134 (2007), pp. 389-395.

Bernini, R, A Minardo, and L Zeni. “Distributed Sensing at centimeter-scale spatial resolution by BOFDA: Measurements and signal processing.” IEEE Photonics J. 2012, 4, 48–56.

Bolognini, G, MA Soto, and FD Pasquale. “Fiber-optic distributed sensor based on hybrid Raman and Brillouin scattering employing multi-wavelength Fabry-Pérot lasers.” IEEE Photonics Technol. Lett. 2009, 21, 1523-1525.

Bolognini, G and MA Soto. “Optical pulse coding in hybrid distributed sensing based on Raman and Brillouin scattering employing Fabry-Pérot lasers.” Opt. Express 2010, 18, 8459-8465.

Brown, GA and AH Hartog. “Optical fiber sensors in upstream oil and gas.” J. Petroleum Technol. 2002, 54, pp. 63-65.

Chen, G, Y Huang, and Y Bao. “Measurement of strain distributions and detection of cracks in unbonded concrete pavement overlays using optical fibers.” Report to MODOT. 2014.

Childs, P, A C L Wong, W Terry and G D Peng. “Measurement of crack formation in concrete using embedded optical fibre sensors and differential strain analysis.” Meas. Sci. Technol. 19, 065301, 2008.

Culverhouse, D, F Farahi, CN Pannell, and DA Jackson. “Potential of stimulated Brillouin scattering as sensing mechanism for distributed temperature sensors.” Electron. Lett. 1989, 25, pp. 913-915.

Deif, A, B Martín-Pérez, B Cousin, C Zhang, X Bao, and W Li. “Detection of cracks in a reinforced concrete beam using distributed Brillouin fibre sensors”. Smart Materials and Structures 19 (2010), pp. 1-7.

Dong, Y, L Chen, and X Bao. “High-spatial-resolution time-domain simultaneous strain and temperature sensor using Brillouin scattering and birefringence in a polarization-maintaining fiber.” IEEE Photon. Technol. Lett. 2010, 22, 1364-1366.

Dong, Y, H Zhang, L Chen, and X Bao. “A 2-cm-spatial-resolution and 2-km-range Brillouin optical fiber sensor using a transient differential pulse pair.” Appl. Opt. 2012, 51, 1229-1235.

Garus, D, T Golgolla, K Krebber, and F Schliep.” Brillouin optical frequency-domain analysis for distributed temperature and strain measurements.” J. Lightwave Technol. 1997, 15, 654–662.

Golgolla, T and K Krebber. “Distributed beat length measurements in single-mode optical fibers using stimulated Brillouin-scattering and frequency-domain analysis.” J. Lightwave Technol. 2000, 18, 320–328.

Hao, L, W Li, N Linze, L Chen, and X Bao. “High resolution DPP-BOTDA over 50 km fiber using return to zero coded pulses.” Opt. Lett. 2010, 35, 1503-1505.

Hartog, AH, DN Payne, and AJ Conduit. “Polarization Optical-Time-Domain Reflectometry: experimental results and application to loss and birefringence measurements in single-mode optical fibers.” Proceeding of the 6th European Conference and Exhibition on Optical Communication (ECOC), York, UK, 16-19 September 1980.

Henault, JM, M Quiertant, S Delepine-Lesoille, J Salin, G Moreau, F Taillade, and K Benzarti. "Quantitative strain measurement and crack detection in RC structures using a truly distributed fiber optic sensing system." Construction and Building Materials 37 (2012), pp. 916-923.

Horiguchi, T, T Kurashima, and M Tateda. "Tensile strain dependence of Brillouin frequency shift in silica optical fibers." IEEE Photonics Technol. Lett. 1989, 1, pp. 107–108.

Hotate, K and Hasegawa T. "Measurement of Brillouin gain spectrum distribution along an optical fiber with a high spatial resolution using a correlation-based technique - Proposal, experiment and simulation." IEICE Trans. Electron. 2000, E83-C, pp. 405-411.

Hotate, K and M Tanaka. "Distributed fiber Brillouin strain sensing with 1cm spatial resolution by correlation-based continuous-wave Technique." IEEE Photonics Technol. Lett. 2002, 14, pp. 179-181.

Hotate, K. "Brillouin scattering accompanied by acoustic grating in an optical fiber and applications in fiber distributed sensing." Proc. SPIE 2011, 7753, pp. 7-10.

Jiang, Y, CKY Leung, M Ng, M Motavalli, G Feltrin, D Gsell. "Delamination detection in an I-section glass fiber reinforced plastic beam with an optical fiber-based stress wave method." Smart Mater. Struct. 18, 065003, 2009.

Juarez, JC, EW Maier, KN Choi, and HF Taylor. "Distributed fiber-optic intrusion sensor system." J. Lightwave Technol. 23(6), 2005, pp. 2081-2087.

Kishida, K and CH Li. "Pulse pre-pump-BOTDA technology for new generation of distributed strain measuring system." Structural Health Monitoring and Intelligent Infrastructure 2006, pp. 471-477.

Kishida, K, CH Li, K Nishiguchi, Y Yamauchi, A Guzik, and T Tsuda. "Hybrid Brillouin-Rayleigh distributed sensing system." Proc. SPIE 2012, 8421, 84212G.

Kishida, K, K Nishiguchi, CH Li, and A Guzik. "An important milestone of distributed fiber optical sensing technology: separate temperature and strain in single SM fiber." Proc. OECC 2009 (14), 1-2.

Kurashima, T, T Horiguchi, and M Tateda. "Distributed-temperature sensing using stimulated Brillouin scattering in optical silica fibers." Opt. Lett. 1990, 15, pp. 1038-1040.

Kingsley, SA and DEN Davies. "OFDR diagnostics for fibre and integrated-optic systems." Electron. Lett. 1985, 21, pp. 434-435.

Lange, DA and HC Shin. "Early age stresses and debonding in bonded concrete overlays." Transportation Research Record 2001, 1778, 174-181.

Leung, CKY, Z Yang, Y Xu, P Tong, SKL Lee. “Delamination detection in laminate composites with an embedded fiber optical interferometric sensor.” Sensors and Actuators A 119, 336-344, 2005.

Li, W, X Bao, Y Li, and L Chen. “Differential pulse-width pair BOTDA for high spatial resolution sensing.” Opt. Express 2008, 16, 21616-21625.

Ling, H, K Lau, L Cheng, and W Jin. “Fibre optic sensors for delamination identification in composite beams using a genetic algorithm.” Smart Mater. Struct. 14, 287–295, 2005.

Lu, Y, T Zhu, L Chen, and X Bao. “Distributed vibration sensor based on coherent detection of phase-OTDR.” J. Lightwave Technol. 28, 2010, pp. 3243-3249.

Martin, AR, GF Fernando, KF Hale. “Impact damage detection in filament wound tubes using embedded optical fibre sensors.” Smart Mater. Struct. 6, 470–476, 1997.

Minakuchi, S, H Banshoya, S Ii and N Takeda. “Hierarchical fiber-optic delamination detection system for carbon fiber reinforced plastic structures.” Smart Mater. Struct. 21, 105008, 2012.

Parker, R, M Farhadiroushan, VA Handerek, and AJ Roger. “A fully distributed simultaneous strain and temperature sensor using spontaneous Brillouin backscatter.” IEEE Photonics Technol. Lett. 1997, 9, 979–981.

Pinto, NMP, O Frazao, JM Baptista, and JL Santos. “Quasi-distributed displacement sensor for structural monitoring using a commercial OTDR.” Optics and Lasers in Engineering 44 (2006), pp. 771-778.

Propst, A, K Peters, M A Zikry, S Schultz, W Kunzler, Z Zhu, M Wirthlin, and R Selfridge. “Assessment of damage in composite laminates through dynamic, full-spectral interrogation of fiber Bragg grating sensors.” Smart Mater. Struct. 19, 015016, 2010.

Qin, Z, T Zhu, L Chen, and X Bao. “High sensitivity distributed vibration sensor based on polarization maintaining configurations of phase-OTDR.” IEEE Photonics Technol. Lett. 23(15), 2011, pp. 1091-1093.

Rogers, AJ. “Polarisation optical time domain reflectometry.” Electron. Lett. 1980, 16, 489–490.

Shimizu, K, T Horiguchi, Y Koyamada, and T Kurashima. “Coherent self-heterodyne detection of spontaneously Brillouin-scattered light waves in a single-mode fiber.” Opt. Lett. 1993, 18, 185-187.

Shin, HC and DA Lange. “Effects of shrinkage and temperature in bonded concrete overlays.” ACI Materials Journal 101 (5), 358-364. 2004.

Shin, AHC and DA Lange. “Effects of overlay thickness on surface cracking and debonding in bonded concrete overlays.” Can. J. Civ. Eng. 39: 304-312. 2012.

Soller, BJ, DK Gifford, MS Wolfe, and ME Froggatt. “High resolution optical frequency domain reflectometry for characterization of components and assemblies.” Opt. Express 2005, 13, pp. 666-674.

Takada, K, A Himeno, and K Yukimatsu. “Phase-noise and shot-noise limited operations of low coherence optical time domain reflectometry.” Appl. Phys.Lett.1991, 59, pp. 2483-2485.

Tsuda, H, J Takahashi, K Urabe. “Damage monitoring of carbon fiber reinforced plastics with Michelson interferometric fiber-optic sensors.” J. Mater. Sci. 34, 4163-4172, 1999.

Wan, KT and C Leung. “Applications of a distributed fiber optic crack sensor for concrete structures.” Sensors and Actuators A 135 (2007), pp. 458-464.

Wegmuller, M, F Scholder, and N Gisin. “Photon-counting OTDR for local birefringence and fault analysis in the metro environment.” J. Lightwave Technol. 2004, 22, pp. 390–400.

Yilmaz, G and SE Karlik. “A distributed optical fiber sensor for temperature detection in power cables.” Sensors and Actuators A 125 (2006), pp. 148-155.

Zeng, X, X Bao, CY Chhoa, TW Bremner, AW Brown, MD DeMerchant, G Ferrier, AL Kalamkarov, and AV Georgiades. “Strain measurement in a concrete beam by use of the Brillouin-scattering-based distributed fiber sensor with single-mode fibers embedded in glass fiber reinforced polymer rods and bonded to steel reinforcing bars.” Applied Optics 41 (2002), pp. 5105-5114.

Zhou, D, W Li, L Chen, and X Bao. “Distributed temperature and strain discrimination with stimulated Brillouin scattering and Rayleigh backscatter in an optical fiber.” Sensors 2013, 13, 1836-1845.

Zou, W, Z He, and K Hotate. “Complete discrimination of strain and temperature using Brillouin frequency shift and birefringence in a polarization-maintaining fiber.” Opt. Express 2009, 17, 1248-1255.

Zou, W, Z He, and K Hotate. “Demonstration of Brillouin distributed discrimination of strain and temperature using a polarization-maintaining optical fiber.” IEEE Photonics Technol. Lett. 2010, 22, 526-528.